Pathogenetic insights from novel mouse models for human epilepsy-associated developmental glioneuronal tumors

Doctoral thesis

to obtain a doctorate (PhD)

from the Faculty of Medicine

of the University of Bonn

Silvia Cases Cunillera

Torregrossa, Spain

2022

Written with authorization of

the Faculty of Medicine of the University of Bonn

First reviewer: Prof. Dr. Susanne Schoch McGovern

Second reviewer: Prof. Dr. Gilles Huberfeld

Day of oral examination: 16.09.2022

From the Institute of Neuropathology

Director: Prof. Dr. med. Torsten Pietsch

Table of contents

List of abbreviations

4E-BP1	Eukaryotic translation initiation factor 4E-binding protein 1
aCSF	Artificial cerebrospinal fluid
aGG	Anaplastic ganglioglioma
BRAF	B-Raf proto-oncogene serine/threonine kinase
CAG	CMV early enhancer/chicken β actin
CNS	Central nervous system
DEG	Differentially expressed gene
E	Embryonic day
FCD	Focal cortical dysplasia
FDR	False discovery rate
GBM	Glioblastoma
GG	Ganglioglioma
GO	Gene Ontology
GFP	Green fluorescent protein
GFAP	Glial fibrillary acidic protein
iRFP	Near-infrared fluorescent protein
IUE	*In utero* electroporation
Ki67	Proliferation marker protein Ki67
MAP2	Microtubule-associated protein
MEA	Multielectrode array
NeuN	Neuron-specific nuclear protein
Olig2	Oligodendrocyte transcription factor 2
P	Postnatal day

PB	PiggyBac
PCA	Principal component analysis
PI3K	Phosphatidylinositol-3-kinase
*p*S6	Phosphorylated ribosomal S6 protein
PLNTY	Polymorphous low-grade neuroepithelial tumor of the young
RFP	Red fluorescent protein
RNA-seq	RNA-sequencing
RSK	Ribosome S6 kinase
SynI	Synapsin I
TME	Tumor microenvironment
TR	Terminal repeat
TSC	Tuberous sclerosis complex
WHO	World Health Organization

1. Introduction

Central nervous system (CNS) tumors comprise a wide spectrum of entities that differ in many regards including molecular genetics, cellular composition and growth kinetics, parameters that are critically affecting the clinical symptoms and course of the disease (Louis et al., 2021) and epileptic seizures are a frequent symptom. A group of heterogeneous glial and glioneuronal tumors has been referred to as long-term epilepsy-associated tumors (LEATs; (Luyken et al., 2004)). They are characterized by a variety of neoplasms with distinct histologic features including astro-, oligodendroglial and glioneuronal neoplasms and account for a significant fraction of childhood brain tumors (Aghajan et al. 2016; Aguilera et al. 2016). Among the LEAT series, gangliogliomas (GGs) represent the most common neoplasms (Blümcke et al., 2016; Blümcke et al., 2017).

1.1. Gangliogliomas

GGs are glioneuronal neoplasms, which constitute not only the highest abundant LEATs but also the most frequently encountered neoplasms in patients with focal, pharmacoresistant temporal lobe epilepsy (Blümcke et al., 2016; Blümcke et al., 2017; Wolf et al., 1994). GGs occur mostly in children and young adults with their mean prevalence at the age of 12 years (Dudley et al., 2015; Zhang et al., 2008). They have an incidence of only 1 - 3 % of all pediatric CNS tumors (Blümcke & Wiestler, 2002; Louis et al., 2016). Although they can arise in different localizations, they are preferentially located within the temporal lobe (Zentner et al., 1994).

Generally, GGs are following a benign biological course subcategorized by the World Health Organization (WHO) as grade I. Less commonly, GGs (1 - 3 %) can acquire malignant features and give rise to anaplastic gangliogliomas (aGGs), which are classified as WHO grade III (Luyken et al., 2004; Wolf et al., 1994).

1.1.1. Neuropathology of GGs

Histologically, GGs are characterized by a biphasic pattern composed of an admixture of neoplastic astroglial and dysmorphic neuronal elements (Hirose et al., 1997). Dysmorphic ganglionic elements are enlarged cells of irregular shapes with frequent bi- and

multinucleation, a large nucleolus and condensed Nissl substance in the soma (**Fig. 1**, (Blümcke & Wiestler, 2002)). These dysmorphic neurons are placed in a disorganized manner and they are sustained and entrapped within an astroglial matrix (**Fig. 1**). The glial component of the tumor may be variable in appearance and represents the neoplastic fraction of GGs (Blümcke & Wiestler, 2002; Luyken et al., 2004). Perivascular lymphocytic cuffs and parenchymal plasma cells are also often present in these tumors (Luyken et al., 2004).

Immunohistochemically, dysmorphic cell elements are strongly positive for microtubule-associated protein 2 (MAP2), neurofilament protein and show peri-somatic accumulation of synaptophysin. The glial component of the tumors strongly binds antibodies against the glial fibrillary acidic protein (GFAP; **Fig. 1**, (Hirose et al., 1997; Luyken et al., 2004; Wolf et al., 1994)).

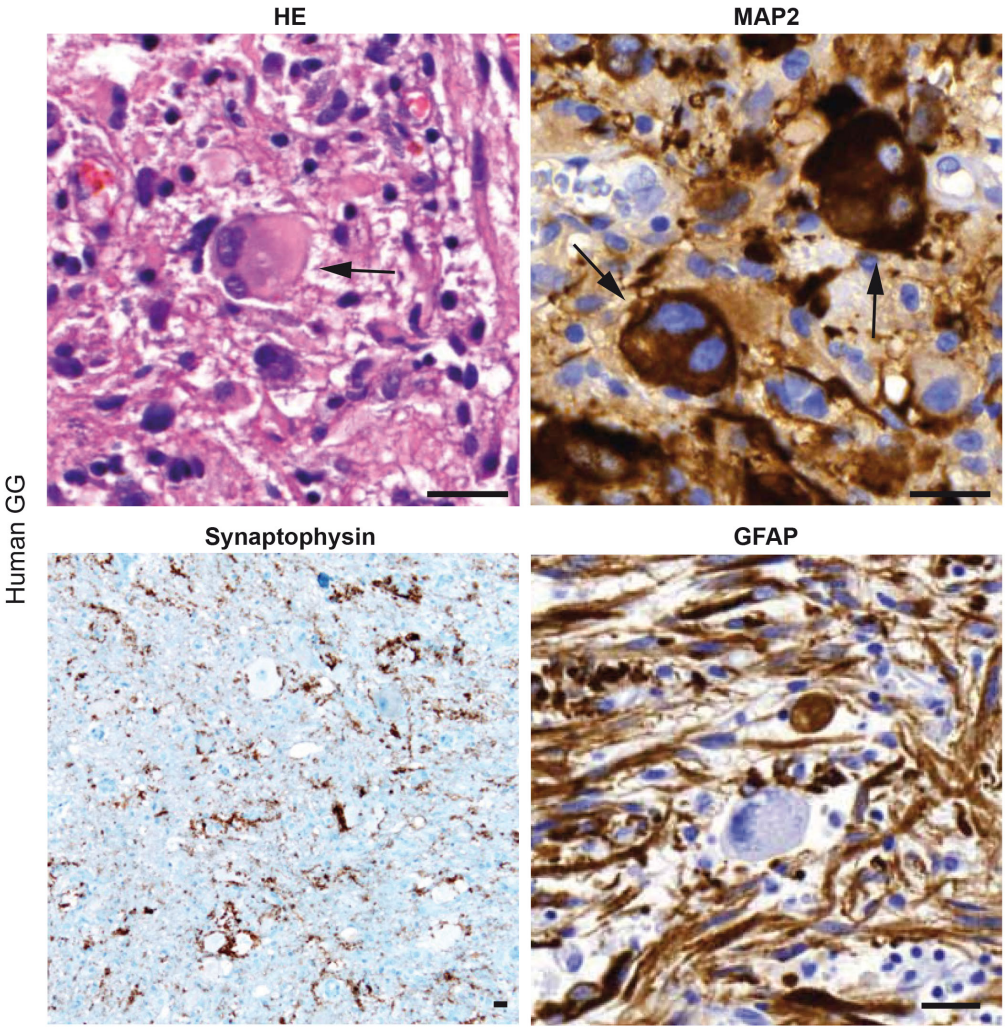

Fig. 1. Immunohistochemical images of human GG. Hematoxylin and eosin (HE) staining depicts the histology/architecture within human GG tissue. Arrow points to a dysmorphic neuron with an enlarged cytoplasm and binucleation (upper left panel). Immunohistochemical reactions with antibodies against MAP2 antigen reveals dysmorphic neurons positive for this antigen (arrows, upper right panel). Representative image from human GGs with immunostaining against synaptophysin exhibit perisomatic reactivity (lower left panel). Image from human GGs stained with antibodies against GFAP reveal the presence of an astrocytic fibrillary matrix around the neuronal component (lower right panel). Human tissue samples were obtained from patients undergoing neurosurgery in Bonn Medical Center. Scale bar, 25 µm.

1.1.2. Molecular pathology of GGs

Mutant *BRAF*^{V600E} represents the most common genetic alteration in GGs (Chappé et al., 2013; Dougherty et al., 2010; Schindler et al., 2011). BRAF is a serine-threonine protein kinase that belongs to the mitogen-activated protein kinase (MAPK) signaling pathway. This pathway is responsible for signal transmission from the cell surface to the nucleus leading to gene expression changes related to tumor growth, differentiation, proliferation and angiogenesis. Indeed, the most common mutation affecting this gene is a missense sequence alteration at the exon 15 leading to a substitution from valine to glutamic acid at the residue 600 of the protein (V600E). This mutation is located within a loop enriched with glycine, which normally is responsible for suppressing BRAF activity. V600E leads to a constitutive increase in the kinase domain activity of the protein and continuous activation of the signaling cascade, which ultimately contributes to uncontrolled cell proliferation, survival and oncogenesis (Davies et al., 2002; Ritterhouse & Barletta, 2015; Wan et al., 2004).

BRAF^{V600E} has been described in a large variety of tumors. The mutation was initially encountered in human melanomas (Davies et al., 2002) and during the last years it has been detected in different types of CNS tumors. So far, the presence of *BRAF*^{V600E} has not been found to have an extensive impact on key clinical parameters in GG patients with a certain limitation of the small sample size of the cohorts under study (Pekmezci et al., 2018).

Koelsche and colleagues immunohistochemically detected BRAF^{V600E} preferentially in neuronal elements as well as only concomitantly in the glial cell fraction of GGs. Whereas BRAF^{V600E}-mediated activation of the MAPK pathway has immediate implications for

neoplastic glial proliferation in GGs (Koelsche et al., 2013), the significance of the acquisition of dysmorphic neuronal features remains enigmatic.

Large dysmorphic neurons represent also a cytological hallmark of focal cortical dysplasias (FCD) type 2 (Taylor et al., 1971; Thom et al., 2005). FCDs type 2 belong to the spectrum of mTORo-pathies (Koh et al., 2018), which defines a group of neurodevelopmental pathologies with alterations affecting the phosphatidylinositol-3-kinase-Akt-mammalian mechanistic target of rapamycin (PI3K/Akt/mTOR) pathway.

The PI3K/Akt/mTOR signaling pathway regulates cell survival under stress conditions. Several receptor tyrosine kinases involved in the detection of extracellular stimuli can further activate PI3K, which translocates to the membrane and integrate signals from the extracellular space (Sánchez-Alegría et al., 2018). PI3K activation triggers the recruitment of several proteins to the membrane, including Akt. The translocation of Akt to the plasma membrane causes the phosphorylation of residues located in its kinase domain leading to protein activation (Alessi et al., 1997; Sarbassov et al., 2005). Akt activation leads to further activation of mTOR, which is a serine/threonine protein kinase involved in the regulation of cell survival, proliferation, apoptosis and autophagy(Alayev & Holz, 2013; Laplante & Sabatini, 2009). Its function depends on the activation of several downstream proteins including the ribosomal protein S6 (S6), which is involved in the translation of mRNA (Thomas et al., 1982). Ultimately, an aberrant increase in the pathway activity leads to alterations in cell growth and proliferation. In fact, diagnostic of mTORo-pathies is regularly performed with immunohistochemical analysis for S6 phosphorylation (Aronica et al., 2007; Baulac, 2016; Crino et al., 2010).

Boer and colleagues documented PI3K/Akt/mTOR pathway activation in human GGs (Boer et al., 2010). Moreover, in a large series of human GGs, $BRAF^{V600E}$ has been suggested to be significantly associated with the presence of *p*S6, as evidence of mTOR pathway activation in dysmorphic neurons (Prabowo et al., 2014). The mTOR upstream protein Akt is a critical mediator in this pathway and its phosphorylation has also been found in the neuronal component of GGs (Schick et al., 2007).

Mutated *BRAF* in GGs has been hypothesized to induce mTOR hyperactivation mediated by crosstalk with MAPK pathway (Blümcke et al., 2016; Samadani et al., 2007). However,

Koh and colleagues developed an epileptogenic glioneuronal neoplasm model by expression of a mutant *BRAF* in murine embryonic cells and they did not observe an increase in *p*S6 levels in this model. Accordingly, mTOR inhibition with Rapamycin did not exert anti-convulsive effects in these mutant epileptic mice (Koh et al., 2018). Thus, the potential role of mTOR pathway activation in GG pathogenesis remains unclear.

1.1.3. Unresolved impact of TP53 in the development of malignant GG variants

Even though GGs generally have a benign clinal course (Thom et al., 2012), occasionally anaplastic (a)GGs (WHO grade III) occur. They represent 1-3 % of GGs (Luyken et al. 2004; Wolf et al. 1994). aGGs are highly associated with epileptic seizures and the tumor progression worsens their refractory status (Zanello et al., 2017). They are characterized by aggressive biological behavior and represent onco- and epileptological challenges (Blümcke & Wiestler, 2002; Kalyan-Raman & Olivero, 1987; Lang et al., 1993; Louis et al., 2016; Pallud et al., 2013; Russell & Rubinstein, 1962).

Histologically, these are characterized by prominent malignant features in the astroglial component with the presence of mitotic activity, cellular atypia, necrosis and microvascular proliferation (Louis et al., 2007, 2016). The correlation of histological anaplasia with clinical outcome parameters is limited so far (Kalyan-Raman & Olivero, 1987; Lang et al., 1993; Luyken et al., 2004), potentially due to only a small case series of aGGs.

BRAF^{V600E} was found in 3/6 neoplasms in a small series of aGGs (Schindler et al., 2011) and alterations affecting *TP53* have been reported in anaplastic GG variants (Hayashi et al., 2001; Pandita et al., 2007). *TP53* encodes a transcription factor, which acts as a tumor suppressor by promoting cell cycle arrest, senescence and apoptosis to avoid uncontrolled propagation of cells with damaged DNA. In fact, this protein is known as ‘guardian of the genome’ (Lane, 1992) and is the most commonly altered tumor suppressor gene in human cancer (Hollstein et al., 1991; Kastenhuber & Lowe, 2017).

Individual aGG cases had an abnormal accumulation of the TP53 protein in the astrocytic component of tumors (Suzuki et al., 2010) and it was reported in concert with the presence of proliferation-related antigen Ki67-labelled cells (Zanello et al., 2017). Some of the few

existing studies and reports also showed that the presence of *TP53* mutation has been found in recurrent malignant neoplasms emerging from primary GGs with an absence of *TP53* alterations (Hayashi et al., 2001; Kim et al., 2003). However, these descriptive data leave the detailed pathogenetic significance of functional TP53 loss for the acquisition of malignant features of GGs to be studied in detail.

1.2. Pathogenetic concepts of GG tumorigenesis

As mentioned above, GGs are histopathologically characterized by an admixture of neoplastic glial and dysmorphic neuronal elements, which has prompted to different potential ontogenetic concepts. 1. Mutant $BRAF^{V600E}$ protein was detected particularly in neuronal cells and concomitantly within the glial cell fraction (Koelsche et al., 2013). Moreover, the expression of the stem cell marker CD34, which in healthy conditions is only expressed during development, is very frequent in GGs (Blümcke et al., 1999; Blümcke & Wiestler, 2002; Deb et al., 2006). These findings support a ‘clonal’ origin, in which both ganglionic and glial cells emerge immediately from a common neural precursor (**Fig. 2**). 2. The second concept predicts that GGs originate from a developmentally compromised or dysmorphic precursor lesion followed by an independent neoplastic transformation of the glial fraction (Thom et al., 2012). The finding of a somatic mutation in the tuberous sclerosis complex 2 (*TSC2*) gene restricted to the glial population of an individual GG has been in line with this pathogenetic concept (Becker et al., 2001).

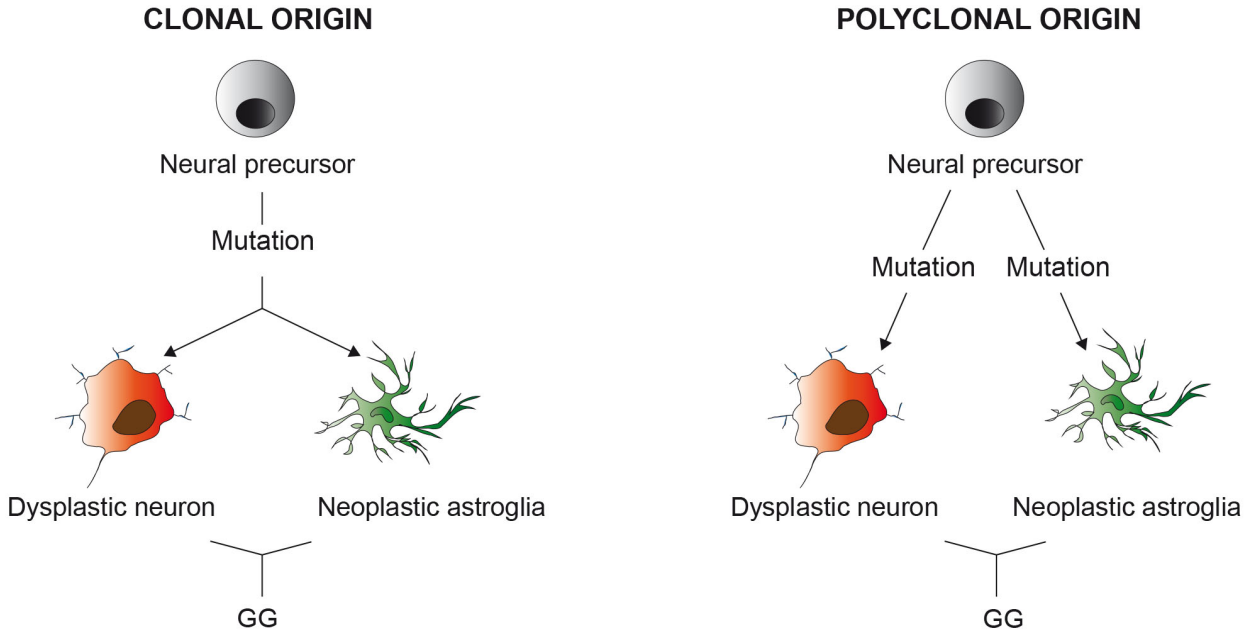

Fig. 2. Schematic representation of the two theories concerning the origin of GGs. Clonal origin supports the idea that GGs arise from a neural precursor altered during development by a single oncogenic event, which acquires the potential of giving rise to dysmorphic neurons and neoplastic astroglia. In contrast, the polyclonal origin supports the existence of two different mutagenic events targeting different cell populations and thereby sustaining that dysmorphic ganglion and neoplastic astroglial cells derive from different precursor cells.

1.3. Epileptological aspects of GGs

GGs represent the most common tumor entity in patients with focal chronic pharmacoresistant epilepsy (Blümcke & Wiestler, 2002; Morris et al., 1993; Wolf et al., 1994). Pharmacological treatment against epilepsy in patients with GGs only seldomly results in seizure-free outcomes and surgical removal of the tumor is the only clinical option.

Previous studies have demonstrated outstanding control of epilepsy after resection of the tumor and between 70 - 90% of the patients have shown seizure-free after surgery. These studies focused on patients with benign GG tumors and with a history of long-term seizures (Haddad et al., 1992; Hu et al., 2012; Luyken et al., 2004; Nishio et al., 2001; Schramm et al., 2001). Surgical removal of GG from patients with a shorter history of epilepsy was proved to lead to even better outcomes (Aronica et al., 2001).

However, resection of the tumor tissue is not directly correlated with seizure control and instead, examination and removal of epileptic tissue are necessary for these patients (Giulioni et al., 2006; Haddad et al., 1992; Im et al., 2002). This aspect further supports the epileptic potential of the peritumoral region (Englot et al., 2012; Giulioni et al., 2006). In this context, cortical dysplasias, which are characterized by abnormal organization of the cortical structures and associated with epilepsy, have been detected in some cases in adjacent areas of GGs (Prayson & Gales, 2015; Saad et al., 2008).

Therefore, further examination of extensive tissue areas around the tumor lesion may be required. For instance, Sommer and colleagues demonstrated that the surgical resection of GG by using a higher sensitive magnetic resonance imaging system led to complete resection of the lesion and an improvement in seizure outcome (Sommer et al., 2015).

Surgical resection of benign GGs results in different seizure outcomes than removal of malignant GGs and a correlation between anaplastic GG and incomplete tumor resection has been shown (Im et al., 2002). In these cases, therapy with radiation after surgery represents a treatment option (Rumana & Valadka, 1998; Silver et al., 1991; Sutton et al., 1983).

Therefore, distinct underlying mechanisms might depend on tumor malignancy. Recent mouse model data suggested that GG neuronal components immediately contribute to hyperexcitability (Koh et al., 2018). Particularly, data obtained from human epilepsy-associated tumor biopsies emphasizes the relevance of the peritumoral area for epileptogenicity (Pallud et al., 2013; Pallud et al., 2014; Wolf et al., 1996).

1.4. Immunological aspects of GGs

Human GG biopsies reveal considerable immune cell infiltration. The presence of perivascular lymphocytic cuffs is a hallmark of these neoplasms and microglia/macrophages and T lymphocytes have been detected in human GG specimens (Lieberman et al., 2019). Differentially regulated inflammation-related microRNAs have also been reported in GGs as well as peritumoral regions harboring epileptogenic potential suggesting an active involvement of inflammatory responses in the generation and/or modulation of seizure activity (Prabowo et al., 2015). Moreover, microglial activation in

GGs has been correlated with subsequent epilepsy duration and seizure frequency (Aronica et al., 2005).

However, the mechanisms by which immune cells are related to epileptic seizures are still elusive. In other pathologies related to epilepsy, several cytokines have been proposed to play a role in this link. For instance, abundant levels of interleukin 1 beta (Il-1β) have been found before seizure onset (Gorter et al., 2006).

Recently, a special focus has been given to the inflammatory mediator C-c motif ligand 2 (CCL2) as a mediator of neuronal hyperexcitability. Pharmacological interference of CCL2 reduced seizure activity in an animal model of mesial temporal lobe epilepsy (Cerri et al., 2016). Interestingly, *CCL2* gene has been found strongly augmented in human GGs (Aronica et al., 2008). In addition, neural stem cells harboring constitutively BRAF activity showed the potential of recruiting microglia via CCL2 (Chen et al., 2019) and the blockage of $BRAF^{V600E}$ led to reduced levels of *Ccl2* in a melanoma mouse model (Knight et al., 2013).

In concert, these findings underline the need for further studies to assess the composition and recruitment of immune cells and their association with neuronal hyperexcitability in GGs.

1.5. Aims

The overall goal of the present study is to gain novel insights in the molecular pathogenesis of GGs by systematically using a transgenic mouse model approach. Intraventricular *in utero* electroporation allows the generation of developmental brain tumor models in mice (Goz et al., 2020; Koh et al., 2018). By applying a similar strategy, the present work aims at understanding the following aspects:

1. Scrutinize whether Akt/mTOR-signaling mediated through constitutively phosphorylated Akt-kinase (*p*Akt) would impact cell biological and neuropathological characteristics of *BRAF*^{V600E}-positive glioneuronal tumors.

2. Characterize the impact of a loss of *Trp53* on the neuropathological as well as phenotypic manifestation of developmental brain tumors harboring *BRAF*^{V600E}.

3. Assess the effect of Akt/mTOR activation as well as *Trp53*-loss on the electrophysiological properties of *BRAF*^{V600E}-positive glioneuronal tumors.

Overall, the present study this study aims to give knowledge on new molecular and functional aspects of developmental brain tumors. *In vitro* and *in vivo* biological experiments were performed in order to address those research concerns.

2. Material and methods

2.1. Experimental models and patient samples

2.1.1. Animals

Mice with a hybrid background (BL6.129-CD1) were used for all experiments described in the current project. Mice with a CD1 background were purchased from Charles River (Strain code: #008462) and B6.129P2-*Trp53*^{tm1Brn}/J mice were obtained from Jackson Laboratories (Stock No: #008462). To increase the IUE efficiency, B6.129P2-*Trp53*^{tm1Brn}/J male mice were bred with CD1 female mice 14 days before the IUE operation. The offspring (BL6.129-CD1 hybrid mice) animals were injected at embryonic day (E) 14 in order to induce brain tumors. To assess the malignancy of the mouse phenotype, the body weight was used as a criterion; mice were considered to exhibit a malignant phenotype as soon as they lost 20 % of their body weight and, in accordance, sacrificed. Mice without showing any malignant phenotype sign were not sacrificed until the age of 110 days. All animals that were not successfully electroporated were not included in the analysis. All experiments from this study were conducted according to the guidelines of the European Union and the University of Bonn Medical Center Animal Care Committee.

2.1.2. Human samples

Human samples were used under patient consent, who gave the agreement about the use of brain tissue for additional studies. Human *BRAF*^{V600E}-positive brain slices (3 GGs and 3 PLNTYs) were obtained from resections of the University of Bonn Medical Center Neurosurgery Program. All the experiments were performed in accordance with the Declaration of Helsinki and approved by the Ethics Committee of the University of Bonn Medical Center.

2.2. Cloning

The sequences of all transgenes required for this project were cloned between two PiggyBac (PB) terminal repeats in the general donor PB plasmid (Wellcome Trust Sanger Institute; Cambridge, UK). First, the UbC promoter from the initial PB plasmid was replaced by the CAG (CMV early enhancer/chicken β actin) promoter and a multiple

cloning site (MCS; 5'-agcttagatctcccgggaccggt-3') was added to the 3´end of the promoter to further clone the transgenes of interest. Second, a fragment containing the mCherry-T2A sequence was amplified.

Table 1 contains information about the DNA plasmids and Table 2 lists the sequence of the primers used for DNA amplification.

Table 1. List of plasmids obtained from collaborators or purchased from a company

Plasmid name	Reference	Manufacturer
$BRAF^{V600E}$-kinase domain	N/A	Dr. David Jones – German Cancer Research Center, Heidelberg
pCDH-CMV-mCherry-T2A-Puro	Cat #72264	Addgene
myr-Akt1-pUSEamp	Cat #17245	Addgene
AAV-GFP/Cre	Cat #49056	Addgene
pCAG-Brainbow3.0	Cat #45176	Addgene
piRFP	Cat #31857	Addgene

Table 2. Sequences of the forward and reverse primers used for cloning

PCR fragment	Direction	Primer 5´-3´sequence	Enzyme	Vector
CAG-MCS	fw	gcgctcgagtcattagttcatagc ccatatatgg	XhoI	pB-CAG-MCS

CAG-MCS	rv	gcgggatccaccggtcccggga gatctaagcttgccaaaatgatga gacagcacaa	BamHI	pB-CAG-MCS
mCherry	fw	gcgggatccatggtgagcaagg gcgaggagc	BamHI	pB-CAG-mCherry
mCherry	rv	gcggaattcctagaagcccttgta cagctc	EcoRI	pB-CAG-mCherry
mCherry-$BRAF^{V600E}$	fw	gcgaagcttggaccaggaatggt gagcaagggcgagg	HindIII	pB-CAG-mCherry-$BRAF^{V600E}$
mCherry-$BRAF^{V600E}$	rv	gcggaattcgtggacaggaaac gcaccat	EcoRI	pB-CAG-mCherry-$BRAF^{V600E}$
myrAkt (pAkt)	fw	gcgggatccatggggagcagca agagcaa	BamHI	CAG-myrAkt
myrAkt (pAkt)	rv	gcggaattcggctgtgccactgg ctgagt	EcoRI	CAG-myrAkt
mCherry-pAkt	fw	gcgaagcttggaccaggaatggt gagcaagggcgagg	HindIII	pB-CAG-mCherry-pAkt
mCherry-pAkt	rv	gcggaattcggctgtgccactgg ctga	EcoRI	pB-CAG-mCherry-pAkt

Cre	fw	gcgaagcttatggccaatttactg accgtac	HindIII	pB-CAG-Cre-mCherry
Cre-(2A)	rv	gcgcccgggggaagcggagag ggcagaggaagtcttctaacatg cggtgacgtggaggagaatccc ggccctgatcgccatcttccagca ggc	SmaI	pB-CAG-Cre-mCherry
$BRAF^{V600E}$	fw	gcgaccggtgaccatggacttga ttagagaccaagg	AgeI	pB-CAG-$BRAF^{V600E}$
$BRAF^{V600E}$	rv	gcggaattcgtggacaggaaac gcaccat	EcoRI	pB-CAG-$BRAF^{V600E}$
pAkt	fw	gcgaagcttgaccatggggtgtat taaatcg	HinIII	pB-CAG-pAkt
pAkt	rv	gcggaattcggctgtgccactgg ctga	EcoRI	pB-CAG-pAkt
Cre	fw	gcgaagcttatggccaatttactg accgtac	HindIII	pB-CAG-Cre
Cre-(2A)	rv	gcggaattccgcagggccggga ttctcctccacgtcaccgcatgtta gaagacttcctctgccctctccgct tccatcgccatcttccagcag	EcoRI	pB-CAG-Cre
$iRFP_{713}$	fw	tcattttggcaagcttatggctgaa ggatccgtcg	HindIII	pB-CAG-$iRFP_{713}$

$iRFP_{713}$	rv	tcatggatccaccggttcactcttc catcacgccgatct	AgeI	pB-CAG-$iRFP_{713}$
Brainbow	fw	cacagaatccaagtcggaact		pB-CAG-Brainbow
Brainbow	rv	ttctcccggtcagctgact		pB-CAG-Brainbow

2.3. Intraventricular *in utero* electroporation

Mice were mated in a coordinated manner for one day, designated as E0. All the embryos were electroporated at E14 in order to target cortical progenitor cells from cortical layer II/III and IV. Isoflurane inhalation was employed in order to anesthetize the pregnant female mice during the whole procedure. 30 min before starting the surgical operation, Buprenorphin (0.05 mg/kg) and Ketoprofen (5 mg/kg) were injected subcutaneously. The DNA solution was prepared at a final concentration of 1.5 µg/µl and further mixed with 1mg/ml Fast Green FCF to visualize the injected solution in the ventricles. A midline abdominal incision was performed on the female mice, and after uterus exposure, the DNA solution was injected into the lateral ventricle of each embryo with the use of a glass capillary pipette and expelled by pressure with a microinjector. A triple-paddle electrode was placed on the head of the embryos and five electric pulses of 45 V were delivered using the CUY21 SC Square Wave Electroporator. Following intrauterine surgery, the incision was closed by sewing the muscle and stitching the skin. After surgery, female mice were subcutaneously injected for three days with Ketoprofen (5 mg/kg).

2.4. Histology and immunochemistry

For histological analysis, hematoxylin and eosin (HE) staining was always performed on 4 µm tissue sections derived from formalin-fixed paraffin-embedded (FFPE) tissue blocks, The brain slices were deparaffinized with a decreasing gradient of ethanol and incubated

5 min in hematoxylin. After rinsing slices for 10 min in water in order to wash out the hematoxylin, sections were immersed in eosin solution for 2 min, followed by 1 min in 100 % ethanol, 2 min in isopropanol (2 times) and 1 min xylene (2 times).

For immunochemical studies, both FFPE-slices as well as free-floating slices were used. For 4 µm FFPE-slices, sections were deparaffinized and incubated with 10 mM citrate buffer in a microwave for 6 min (2 times) for antigen retrieval. After washing slices in water for 1 min, incubation in 1 % H_2O_2 for 30 min was performed to quench the peroxidase activity. To block and minimize unspecific antibody binding, a blocking solution composed of 5 % normal goat serum (NGS) in phosphate-buffered saline (PBS) was used. After blocking for 30 min at 25 °C, slices were incubated with the corresponding primary antibodies for 30 min at 4 °C. After washing with PBS, brain sections were treated with biotinylated anti-mouse or anti-rabbit secondary antibodies, which were finally detected by using a Vectastain kit and diaminobenzidine (DAB) staining, followed by a counterstaining with hematoxylin.

For the immunofluorescence analysis of free-floating slices, first mice were decapitated, and the brains were quickly removed and sectioned by using a vibratome. The resulting slices were fixed with 4 % formaldehyde overnight at 4 °C. A washing step with PBS was performed and slices were incubated in a blocking solution containing 0.1 % Triton-X, 0.1 % Tween-100 and 2 % Bovine serum albumin (BSA) in PBS for 1 h at 25 °C prior to overnight incubation with the corresponding primary antibodies (**Table 3**). After washing with PBS, sections were incubated with an Alexa Fluor-conjugated antibody diluted in the blocking solution for 2 h at 25 °C. DAPI (1:00) staining for 20 min at RT was used to visualize the cell nuclei. All slices were finally mounted in Mowiol.

Table 3. Primary antibodies used for the immunohistochemical studies.

Antibody	Species	Reference	Manufacturer	Dilution
GFAP	mouse	G3893	Sigma Aldrich	1:500
Ki67	rabbit	16667	Abcam	1:50
MAP2	rabbit	188002	Synaptic Systems	1:200

NeuN	mouse	MAB377	Millipore	1:500
Synapsin 1	mouse	106011	Synaptic Systems	1:200
Iba1	rabbit	019-19741	Wako	1:1000

2.5. Fluorescent microscopy and imaging

The visualization and subsequent imaging of fluorescently labeled brain sections was performed by using Confocal Microscope Nikon Eclipse. For the brain slices expressing the brainbow construct, GFP (Ex: 488 nm/ Em: 500-550 nm) and RFP (Ex: 561 nm/ Em: 570-620 nm) channels were simultaneously used to discern the color-coded cell clones. Z-stack images were acquired at 1 µm intervals.

The sections stained either with HE or though DAB (1 µm thick) were imaged with the Mirax Scan digital microscope slide scanner. Higher magnification images from representative regions were taken with the Case Viewer 2.3 Software after a detailed visualization of the tumor lesions.

2.6. Quantitative assessment from immunolabeled slices

To quantify the number of cells positive for *p*S6 and Ki67 from immunolabeled brain slices, the following quantitative analysis was used. First, the tumor region was located within the slice and by using the light microscope pictures were taken from several tumor regions comprising areas of 9.4 mm^2. ImageJ software was used to assess the resulting images and the Cell Counter Plugin was used to quantify labeled (L) and non-labeled (NL) cells according to the presence or absence of the proteins by the tumor cells. The cells from blood vessels or from their walls were excluded from the analysis. Once the number of positive and negative cells within the tumor was quantified, the labeling index (LI) was obtained by dividing the L cells by the total number of cells (L+NL).

2.7. Near-infrared *in vivo* imaging

Mice IU-electroporated with CAG-iRFP together with the vectors coding for the respective oncogenes were *in vivo* monitored at postnatal day 10, 20 and 45. Mice received a

subcutaneous injection of Buprenovet (5 mg/kg) 30 min before the surgery and were anesthetized by inhalation with isoflurane for induction and maintenance during the whole imaging. Previous experiments performed in the lab reported that the signal emitted from the iRFP^{713} cannot be visualized through the brown skin of CD1/BL6 animals. Therefore, the skin from the head was cut in order to expose the skull. The Pearl Impulse Small Animal Imagining System (LI-COR) was used as the imaging device and the fluorescent signals were collected and further quantified by using the Image Studio Lite Quantification Software. The skin from the head was immediately sewed and animals were put back in their respective cages.

2.8. Multielectrode array (MEA) application on acute brain slices

2.8.1. Preparation of acute slices

Tumor mice were decapitated after having been deeply anesthetized by isoflurane inhalation. The brains were quickly removed and immersed in ice-cold carbogen-bubbled cutting solution. Brains were subsequently glued on the vibratom tray and further sliced (300 µm). After cutting the whole brain, all the slices were carefully transferred to an interphase chamber containing carbogen-bubbled cutting solution placed in a water bath at 35 ºC and incubated for 30 min. Tumor brain slices were then transferred into an interphase chamber containing carbogen-bubbled artificial cerebrospinal fluid (aCSF) and incubated for at least 1 h at room temperature in the dark. The resulting acute brain slices were used for the recording. Transference of the slices was in all cases performed by using glass Pasteur pipettes to reduce the tissue damage. The cutting solution contained (in mM) 87 NaCl, 2.5 KCl, 1.25 NaH_2PO_4, 7 $MgCl_2$, 0.5 $CaCl_2$, 25 $NaHCO_3$, 25 D-glucose and 75 sucrose. The aCSF solution contained (in mM) 124 NaCl, 3 KCl, 1.25 NaH_2PO_4, 2 $MgCl_2$, 2 $CaCl_2$, 26 $NaHCO_3$ and 10 D-glucose. The pH of the cutting and the aCSF solutions was adjusted while the liquid was carbogen-bubbled.

2.8.2. MEA recordings and data analyses

Brain slices were carefully placed onto a 64-electrode MEA well from a 6-well plate by using a needle. A fluorescent microscope was used to visualize and further locate the slices according to the fluorescence-expressing tumor tissue on the electrodes. For all the

slices, the tissue was placed so that all electrodes were covered with both fluorescent-tumor and non-fluorescent tissue. After placing the slices, a platinum grid was settled on the top of the slices to maintain them fixed onto the electrode surface. For the whole recording time, slices were incubated in aCSF oxygenated with carbogen in the MEA device. AxIS software was employed to record the spontaneous activity of the slices for 15 min. After that, pictures from the tumor brain slices were taken with an inverted microscope in order to further correlate the brain slice location with the activity.

The analysis of the spontaneous activity was based on the number of spikes per electrode according to the categories. Electrodes were first classified according to the region of the slice they were in direct contact to: Tumor IUE (electrodes in contact with tissue emitting fluorescence, Peri-IUE (electrodes adjacent to the Tumor IUE showing, in some cases, sparse fluorescence) and non-IUE Surrounding tissue (electrodes with absence of fluorescent expression). The number of spikes per category was quantified by dividing the sum of the number of spikes from the category-related electrodes by the number of the total electrodes in the specific category. The fraction of spikes per category was quantified by normalizing the number of spikes per category within the same slice. We, therefore, excluded the slices which did not contain one of the categories. A threshold of 6x standard deviation of the baseline was set with the AxIS Software for the detection of the spike signal.

2.9. Bulk RNA sequencing from tissue

2.9.1. RNA extraction and sequencing

RNA was isolated from the brain tissue of *BRAF*^{V600E}/*p*Akt tumor animals at P110 and *BRAF*^{V600E}/*p*Akt/*Trp53*^{KO} at P40. Total RNAs from tumor and control tissue were isolated using the RNeasy Micro kit following the manufacturer´s instructions and finally diluted in RNAse free water. The quality and concentration of the final RNA solution was measured by using a Nanodrop spectrophotometer and the Qubit RNA HS Assay Kit by using the Qubit 2.0 Fluorometer. RNA was subsequently transcribed to cDNA. After cDNA amplification, libraries for Illumina were prepared using QuantSeq 3´mRNA-Seq Library Preparation Kit. In order to ensure an equimolar ratio between samples, the TapeStation 2200 was used to measure them. Finally, the sequencing was performed by the HiSeq

2500 sequencer with 1x50 bp single-end reads and a depth of 10 millions reads per sample (see **Fig. 3**).

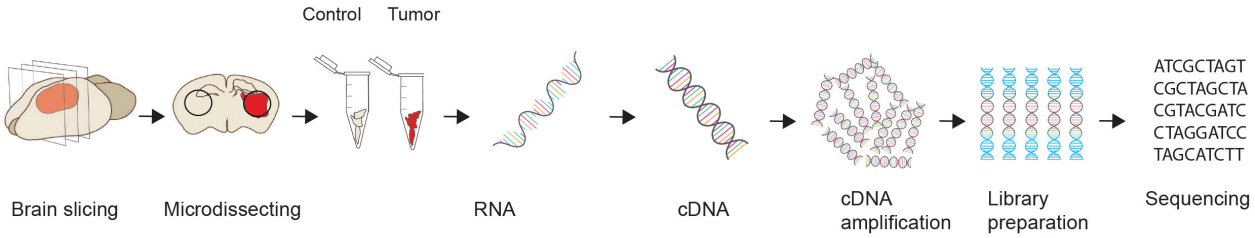

Fig. 3. Schematic workflow of RNA sequencing procedure. Brain tissue (from both control and tumor) is microdissected according to fluorescent expression. RNA isolation is followed by reverse transcription to generate cDNA, which is amplified. After library preparation, cDNA is sequenced.

2.9.2. Bioinformatic analysis

After RNA sequencing, the reads were mapped to the GRCm38/mm10 mouse genome using the STAR aligner v2.4.0.1 (Dobin et al., 2013) following the quality control and trimming. The alignment using the ENSEMBL transcript annotation files and featureCounts v.1.5.3 (Liao et al., 2014) were used to create the matrix containing the number of read counts per single gene. All genes with a low number of reads were excluded and the count matrix was normalized. A Linux-based computer system was used to perform all NGS bioinformatic analysis. The following R/Bioconductor packages were used: (1) Rsubread (Liao et al., 2013) for alignment and quantification of RNA sequencing reads, (2) edgeR (Robinson. et al., 2010) for differential expression analysis and (3) limma (Ritchie et al., 2015) for analysis of gene expression data. The differential gene expression analysis was performed with total number of 17.511 genes and the normalized data were used for fitting linear models. All genes with false discovery rate (FDR) less than 0.05 were considered differential expressed and a principal component analysis (PCA) was generated on them in order to visualize transcriptomic relationships within and between tumor and control samples in a two-dimension-based graph. Heat maps were generated from the normalized counts per gene.

2.10. Statistical analysis

Statistical tests applied to the experiments were performed by using GraphPrism software on the original values. In all cases, the mean of the values was plotted as ± SEM. For differential gene expression comparing tumor and control samples, FDR < 0.05 was used to find the respective up and downregulated genes for bulk RNA-seq. Concerning the quantitative analysis of *p*S6 and Ki67 within the tumor region, the labeling index (LI) was compared across tumor models by using One-Way ANOVA followed by Bonferroni´s Multiple Comparison Test. In the case of survival analysis, the Log-Rank test statistical analysis was applied to the Kaplan-Meier survival curves. Data visualization was performed with GraphPrism, Igor 64 and R Studio.

3. Results

3.1. Neuropathological spectrum of 1-, 2- and 3-hit tumors neoplasms

As an attempt to generate neuroepithelial-like murine brain neoplasms, the intraventricular *in utero* electroporation (IUE) approach was used to transfect neural progenitors *in vivo* (Kolk et al., 2011; lo Turco et al., 2009). After uterus exposure at embryonic day 14 (E14), the plasmid DNA solution is injected into the lateral ventricle of the embryonic brain and the subsequent application of an electric shock allows the DNA to penetrate the cell cytoplasm of the neurogenic population (**Fig. 4**).

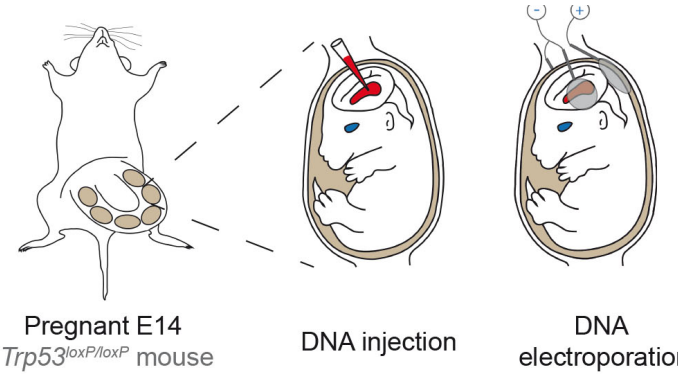

Fig. 4. IUE technical approach. Schematic drawing illustrating the IUE technique. Following uterus exposure at embryonic day 14 (E14), the DNA is injected directly into the lateral ventricle and 5 electrical pulses with an intensity of 40V and a length of 50 ms are applied. Data shown in this figure contributed to Supplementary Figure 1 in Cases-Cunillera et al., 2022.

To avoid the loss of the plasmids during cell division, IUE was further combined with the piggyBac (PB) transposon system, which allows the insertion of the transgenes into the mouse genome and results in a stable expression through the radial glial progenitor cell lineage (lo Turco et al., 2009; Siddiqi et al., 2014). This system consists of a donor plasmid, coding for the gene of interest flanked by two piggyBac terminal repeats (PB-TR) and a helper plasmid expressing the transposase, which recognizes the TR and integrates the transgene into the genome.

3.1.1. Histological characterization of developmental murine brain tumors harboring *BRAF*^{V600E} with and without mTOR activation.

In order to study systematically the status of mTOR pathway activation in *BRAF*^{V600E} positive tumors, initially human GGs characterized by a glioneuronal phenotype (**Fig. 5A**, upper panels), as well as PLNTYs with an oligodendrocyte-like major component were analyzed (**Fig. 5A**, lower panels).

Together with *BRAF*^{V600E}, activation of the Akt/mTOR signaling pathway has been detected in GGs. As a surrogate marker, the downstream mTOR pathway *p*S6 protein component was analyzed by immunohistochemistry; the results confirmed the previously reported *p*S6 activation in human GGs (**Fig. 5A**, right upper panel) (Becker et al., 2006; Boer et al., 2010). In contrast, *p*S6 was almost absent in human PLNTYs (**Fig. 5A**, right lower panel). In order to test for potential effects of PI3K/mTOR pathway activation in concert with *BRAF*^{V600E} systematically in a mouse model, *BRAF*^{V600E} and *p*Akt piggyBac transgenes under the control of the robust and constitutively active cytomegalovirus early enhancer/chicken β actin (CAG) promoter (PB-CAG-BRAF^{V600E}) were co-IU-electroporated together with the piggyBac transposase (pBase; N = 5). To keep track of the targeted cells, the sequence coding for the red fluorescent protein mCherry was integrated into the piggyBac donor transposons (**Fig. 5B**). The further histological analysis of these brains (P110) showed the presence of neoplasms. In contrast, the control animals IU-electroporated with mCherry alone did not show any histological malformation (data not shown). The resulting tumors (further referred to as *BRAF*^{V600E}/*p*Akt or 2-hit model) resembled human GGs and were characterized by (1) large dysmorphic neurons, sometimes binucleated, intermingled within (2) a neoplastic astroglial fibrillary matrix (**Fig. 5C**, upper panel).

To evaluate whether the IUE at E14 of only *BRAF*^{V600E} would be sufficient to trigger tumor development (**Fig. 5B**), a histological assessment of brains was carried out at P110 and the corresponding analysis revealed the presence of circumscribed lesions, further designated as *BRAF*^{V600E} or 1-hit model (n = 8). Even though *BRAF*^{V600E} alone failed to induce lesions with characteristic neuropathological features of glioneuronal tumors, it triggered the development of neoplasms composed of oligoid-like cells, recapitulating

features of PLNTYs (**Fig. 5C**, lower panel). Of note, mice IU-electroporated with only *p*Akt (n = 6) did not show any signs of tumorigenesis at P110.

For both *BRAF*^{V600E}/*p*Akt- and *BRAF*^{V600E}-induced neoplasms, the activation of the Akt/mTOR signaling pathway within the tumor area was verified by performing immunohistochemistry against *p*S6. Whereas *BRAF*^{V600E}/*p*Akt tumor cells showed a strong expression of *p*S6 (**Fig. 5D**, upper panel), *p*S6 was barely encountered within *BRAF*^{V600E}-induced lesion (**Fig. 5D**, lower panel). The number of *p*S6 positive cells among the IU-electroporated cell population was significantly higher in *BRAF*^{V600E}/*p*Akt tumors compared to the tumors induced with only *BRAF*^{V600E} (**Fig. 5E**). Additionally, the activation of the MAPK signaling cascade in *BRAF*^{V600E}/*p*Akt tumors was assessed. For this purpose, the levels of ERK1/2 phosphorylation were quantified from protein lysates extracted from *BRAF*^{V600E}/*p*Akt and control microdissected brain tissue at P70 (n = 3). The western blot results showed significantly higher levels of pMEK1/2/MEK in *BRAF*^{V600E}/*p*Akt tumor compared to control tissue (**Fig. 5F** and **G**).

In parallel, the combinatorial effects of *p*Akt and *BRAF*^{V600E} transgene expression were tested with western blot against the downstream mTOR components *p*S6 and eukaryotic translation initiation factor 4E-binding protein 1 (4E-BP1) in neuroblastoma NS20Y cells. The subsequent quantification showed a higher increase of phosphorylation at both S235/6 and S240/4 residues of the S6 protein in *BRAF*^{V600E}/*p*Akt-transfected cells compared control cells, only transfected with mCherry (n = 4 per group; **Fig. 5H**). In contrast, transfection of *BRAF*^{V600E} alone was not sufficient to induce an increase in *p*S6 protein levels. The levels of p4E-BP1/4E-BP1 were also assessed and activation was not observed after transfection of neither *BRAF*^{V600E} nor *BRAF*^{V600E}/*p*Akt (**Fig. 5H)**. These results suggest that both pathways cooperate in the activation of the Akt/mTOR signaling pathway causing downstream activation of S6.

To verify the potential of *BRAF*^{V600E} to activate the MAPK pathway *in vitro*, Western blot analysis for downstream effector proteins of MAPK signaling pathway was performed after transfection with control, *BRAF*^{V600E} or *p*Akt. The subsequent quantification revealed that the cells transfected with *BRAF*^{V600E} manifested a significant increase in the

pBRAF/BRAF, pERK1/2/ERK1/2 and pMEK1/2/MEK1/2 protein levels, compared to control- and *p*Akt-transfected cells (n = 5; **Fig. 5I**).

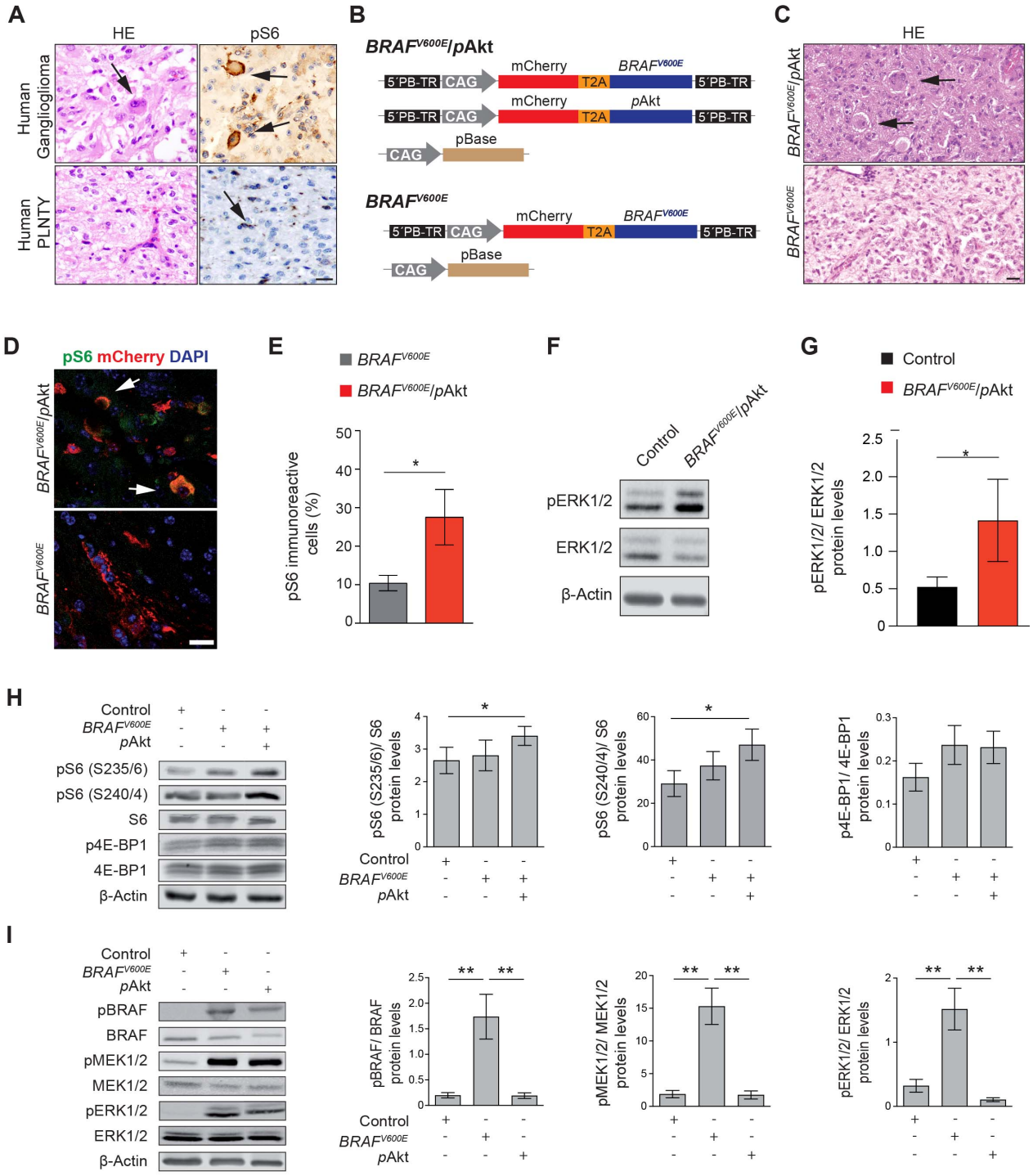

Fig. 5. Evaluation of mTOR pathway activation in human GG samples and verification of the *p*Akt capability of activating the downstream mTOR pathway. (A) Hematoxylin and eosin (HE) staining (left panels) of human GG (upper panel) and human PLNTY (lower panel) brain slices. Human GG exhibits large dysmorphic neurons (arrow) within a neoplastic glial component and PLNTY is

composed of oligoid-like cells. Staining against *p*S6 (right panels) of human GG (upper panel) and human PLNTY (lower panel) brain slices. Arrows point to strong *p*S6 immunolabeled cells within *BRAF*^{V600E}/*p*Akt (upper panel). Scale bar, 100 µm. (B) Schematic representation of the donor plasmids used for IUE: PB-CAG-BRAF^{V600E} and –*p*Akt (further referred to as *BRAF*^{V600E}/*p*Akt) and PB-CAG-BRAF^{V600E} (further named as *BRAF*^{V600E}) as well as the piggyBac transposase (CMV-pBase). In order to keep track of the IU-electroporated cells, the donor plasmid also contains a red fluorescent protein (mCherry) sequence separated from the transgenes by a T2A fragment. (C) Representative HE-stained sections from *BRAF*^{V600E}/*p*Akt (upper panel) and *BRAF*^{V600E} (lower panel) induced neoplasms. Scale bar, 25 µm. (D) Immunohistochemistry of the *p*S6 epitope in *BRAF*^{V600E} and *BRAF*^{V600E}/*p*Akt tissue. Arrows point an IU-electroporated cell positive for *p*S6 in *BRAF*^{V600E}/*p*Akt tumor (n = 5, each). Scale bar, 25 µm. (E) Quantitative analysis of *p*S6-labeled cells among IU-electroporated population. Note the higher amount of *p*S6 positive cells in *BRAF*^{V600E}/*p*Akt, compared to *BRAF*^{V600E}, neoplasms. (F) Western blot analysis of pERK1/2 and ERK1/2 protein levels from control and *BRAF*^{V600E}/*p*Akt tissue. (G) Quantification of pERK1/2/ERK1/2 protein levels in control and *BRAF*^{V600E}/*p*Akt conditions. Two-tailed unpaired t-test. (H) Protein level quantification of pS6(S235/6)/S6, pS6(S240/4)/S6 and pE4-BP1/4E-BP1 from NS20Y cells after transfection with Control, *BRAF*^{V600E} and *BRAF*^{V600E}/*p*Akt detected by western blot analysis (n = 4). The left panel shows the corresponding immunoblots. (I) Bar graphs showing the protein levels of pBRAF/BRAF, pERK1/2/ERK1/2 and pMEK1/2/MEK1/2 (n = 5). The left panel shows the representative immunoblots. Normalization against β-Actin protein levels was used as a loading control. Data are represented as mean ± SEM. One-Way ANOVA followed by Tukey´s multiple comparison test, *p < 0.05; **p < 0.01. Data shown in this figure were modified from Cases-Cunillera et al., 2022.

3.1.2. Immunohistochemical analysis of *BRAF*^{V600E} and *BRAF*^{V600E}/*p*Akt neoplasms

The tissue composition of *BRAF*^{V600E}/*p*Akt- and *BRAF*^{V600E}-induced neoplasms was further characterized by immunofluorescence. The induced neoplasms were co-stained against the MAP2 and GFAP to visualize the neuronal and glial components, respectively. While the staining of *BRAF*^{V600E}/*p*Akt tumors highlighted enlarged dysmorphic MAP2-positive cells placed in a dense astroglial matrix immunopositive for GFAP, *BRAF*^{V600E} tumors were composed of oligoid-like MAP2-labelled cells and a sparser astrocytic component with reactive features (**Fig. 6A**). As an attempt to further determine the involvement of the glial population in the tumorigenic process of both induced neoplasms, the tumor tissue was stained with antibodies against mCherry (a marker for IU-electroporated cells) and GFAP. Consistent with the glioneuronal features shown by *BRAF*^{V600E}/*p*Akt, the results exhibited colocalization between mCherry and GFAP only in *BRAF*^{V600E}/*p*Akt- and not in *BRAF*^{V600E}- induced tumors (**Fig. 6B**). Furthermore, the proliferation-related antigen Ki67 in *BRAF*^{V600E} tumors did not co-label with GFAP in IU-electroporated cells (visualized by mCherry expression), indicating that Ki67-/GFAP-positive cells in these tumors rather represent reactive astrocytes than glial tumor cells

(**Fig. 6C**). In contrast, some IU-electroporated cells positive for GFAP as well as Ki67 were found in *BRAF*^{V600E}/*p*Akt neoplasms, suggesting a neoplastic nature of the glial component (**Fig. 6C**). Finally, the immunofluorescent analysis of the neuron-specific nuclear protein (NeuN; **Fig. 6D**) and oligodendrocyte transcription factor 2 (Olig2) revealed colocalization with mCherry-IU-electroporated cells in *BRAF*^{V600E}/*p*Akt tumors. In contrast, mCherry-positive *BRAF*^{V600E} cells only showed positivity for Olig2 (**Fig. 6E**).

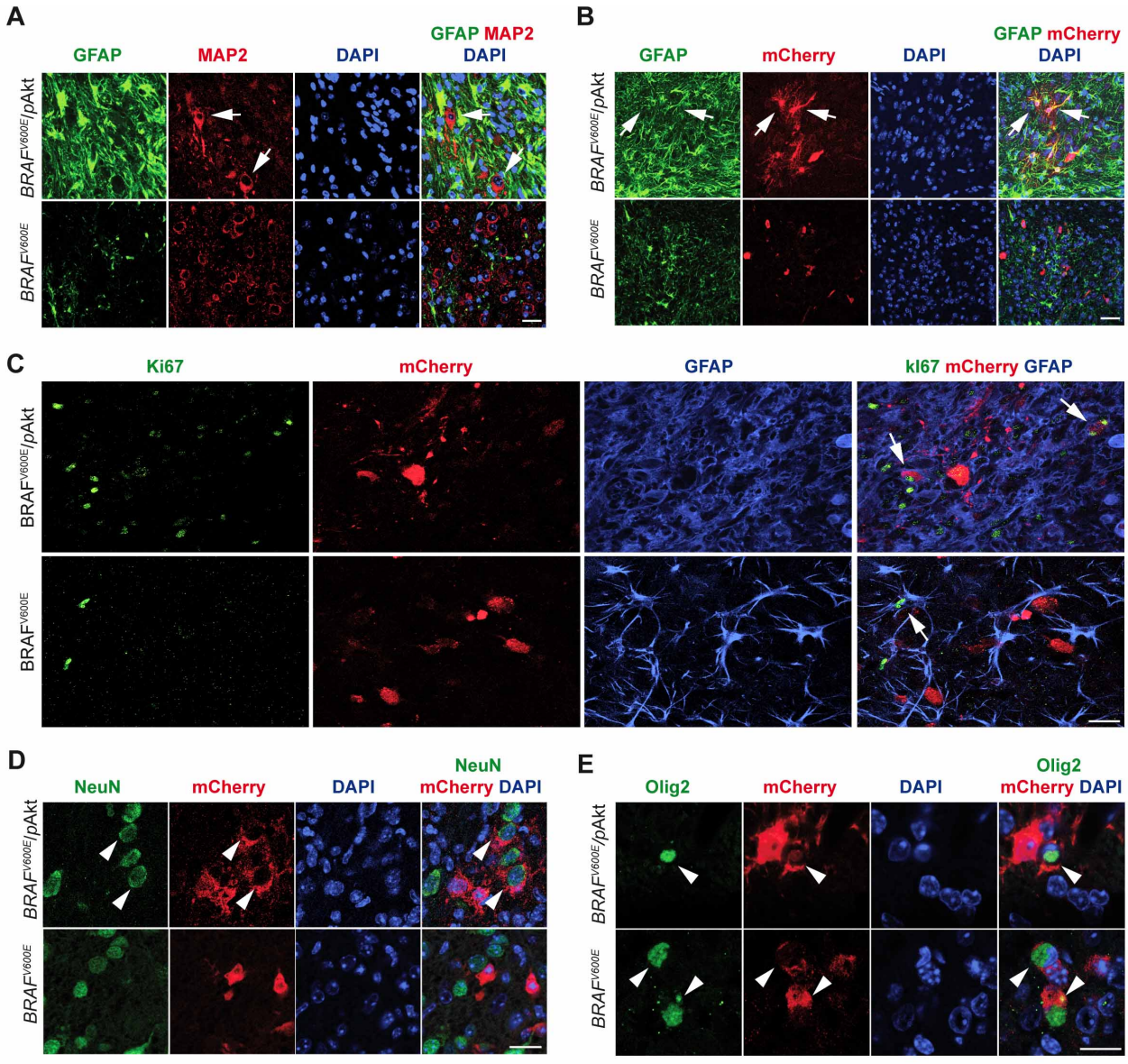

Fig. 6. Immunochemistry of *BRAF*^{V600E}/*p*Akt and *BRAF*^{V600E} neoplasms stained for GFAP, MAP2, NeuN and Olig2. (A) Double staining against GFAP and MAP2. Arrows point to large neurons positive for MAP2 in *BRAF*^{V600E}/*p*Akt neoplasms. Scale bar, 25 µm. (B) Co-staining against GFAP and mCherry of tumor slices. Note that the GFAP immunolabeling of mCherry-positive IU-electroporated cells is exclusively found in *BRAF*^{V600E}/*p*Akt neoplasms (arrows; upper panels). Scale bar, 25 µm (C) Staining for Ki67, mCherry and GFAP. Note the presence of astrocytes

positive for Ki67 and mCherry (arrows) restricted to the *BRAF*^{V600E}/*p*Akt tumor variant. Scale bar, 25 µm. (D) Double immunohistochemical reaction with NeuN and mCherry-positive IU-electroporated cells within *BRAF*^{V600E} and *BRAF*^{V600E}/*p*Akt. Colocalization of NeuN and mCherry-positive cells only in *BRAF*^{V600E}/*p*Akt induced tumor cells. Scale bar, 25 µm (E) Assessment of expression of Olig2 and mCherry proteins showing the presence of IU-electroporated cells positive for Olig2. Scale bar, 25 µm. Data shown in this figure were modified from Cases-Cunillera et al., 2022.

Overall, these results give further evidence that *BRAF*^{V600E} expression in neural precursor cells triggers PLNTY-like tumors in mice, while the generation of GG-like neoplasms only occurs when *BRAF*^{V600E} is expressed concomitantly with activation of the Pi3K/mTOR signaling cascade.

3.1.3. Neuropathological characteristics of tumors induced by *BRAF*^{V600E}, *p*Akt and *Trp53* knockout

Even though GGs are normally indolent tumors, a small percentage of them can undergo malignant transformation (Luyken et al., 2004; Miller et al., 1993; Selvanathan et al., 2011; Wolf et al., 1994). The resulting tumors (WHO grade III) are known as anaplastic GGs (aGGs) and generally the glial component is characterized by astrocytes with malignant features (Louis et al., 2016). Due to the low number of cases, the literature is very poor and inadequately documented. This makes their molecular as well as clinical understanding extremely challenging. According to previous studies from human samples, aGGs have been associated with alterations affecting the tumor suppressor gene *TP53* (Hayashi et al., 2001; Pandita et al., 2007). Therefore, as an attempt to test the influence of *Trp53* loss on the malignant phenotype of mouse GGs, *Trp53*$^{loxP/loxP}$ mice were IU-electroporated with plasmids encoding *BRAF*^{V600E}, *p*Akt and Cre-recombinase at E14 (**Fig. 7A**). The injection of Cre into *Trp53*$^{loxP/loxP}$ living cells triggers the genomic deletion of *Trp53*.

The histopathological analysis of the resulting brains at P30 (further referred as *BRAF*^{V600E}/*p*Akt/*Trp53*^{KO} or 3-hit model) revealed the presence of diffuse neoplasms with a high potential of invasion and proliferation, assessed by immunolabeling against Ki67 (**Fig. 7B**). The resulting tumors were composed of a high proportion of dysmorphic neurons, with sometimes bi- or even multi-nucleation, intermingled within a highly dense neoplastic glial component (**Fig. 7C**). The immunostaining against the neuronal-specific

marker synapsin I (SynI) revealed the presence of giant IU-electroporated neurons (visualized by mCherry fluorescent marker; **Fig. 7D**). Furthermore, co-labeling between GFAP and Ki67 was found in IU-electroporated cells, indicating a tumorigenic role of the glial component (**Fig. 7E**).

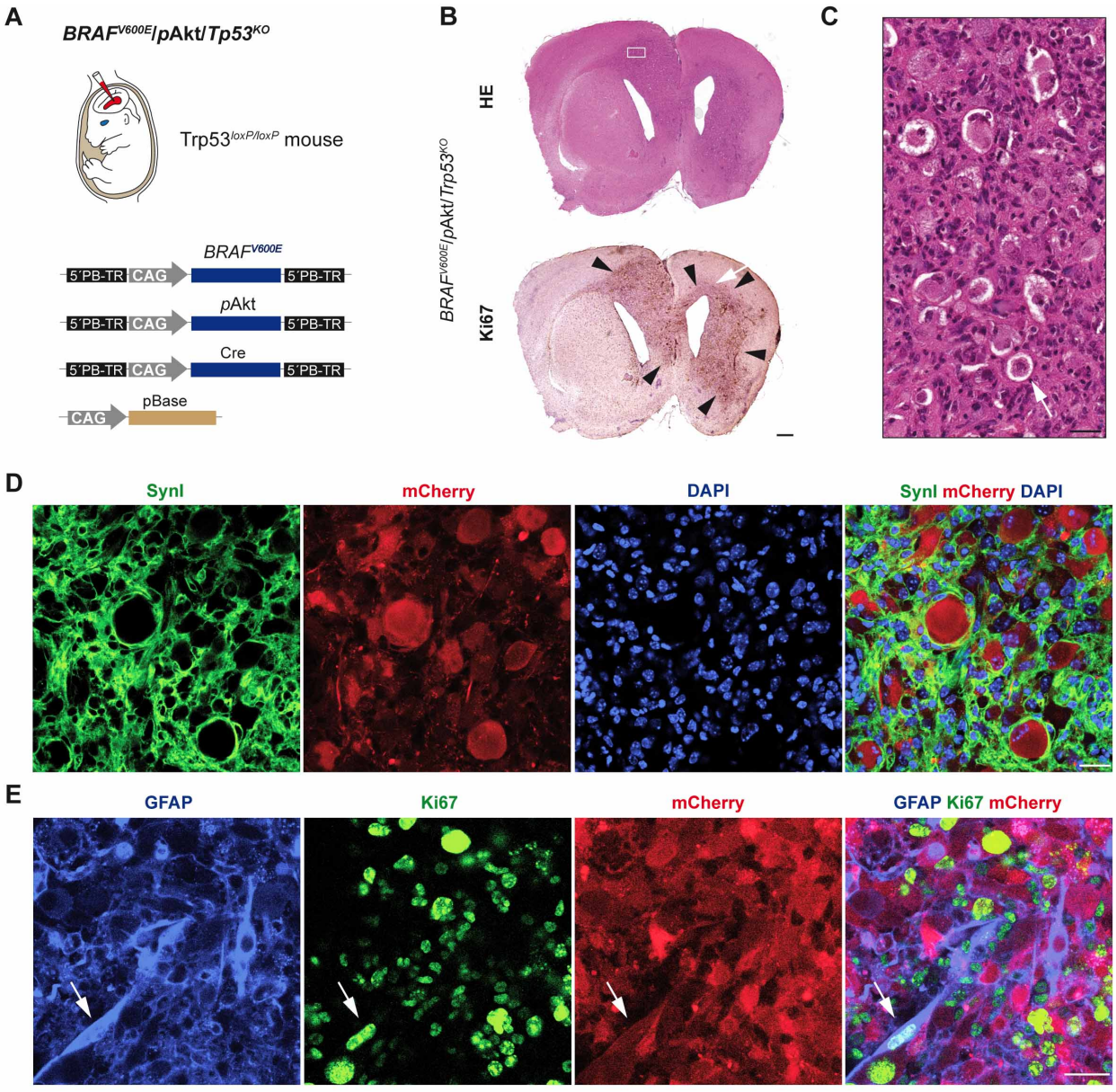

Fig. 7. Immunohistological characterization of *BRAF*^{V600E}/pAkt/*Trp53*^{KO} neoplasms. (A) Scheme of the piggyBac donor plasmids used for IUE of *Trp53*$^{loxP/loxP}$ mice: PB-CAG-BRAF^{V600E}, –*p*Akt and Cre. Injection of Cre in *Trp53*$^{loxP/loxP}$ mice leads to *Trp53* knockout (*Trp53*^{KO}). mCherry sequence is integrated into all plasmids to track the injected cells. Genomic integration of the DNA sequences is facilitated by the co-IUE with the piggyBac transposase (pBase). (B) Representative hematoxylin and eosin (HE; left panel) and Ki67 (right panel) stainings of *BRAF*^{V600E}/*p*Akt/*Trp53*^{KO}

brain sections. The black arrows indicate the invasive margin of the neoplasm. Scale bar, 500 µm (C) Higher magnification image from A of the neoplasm evidences a high number of dysmorphic neurons (white arrows), with sometimes binucleation (white arrow), placed within a dense astroglial component. Scale bar, 25 µm. (D) Staining against SynI shows a positive signal around the cell bodies of the neuronal component, which is composed of large and sometimes bi or multi-nucleated neurons. Scale bar, 25 µm. (E) Double immunostaining against the astroglial-like marker GFAP and the proliferation-related antigen Ki67 evidences a highly proliferative/neoplastic glial component in *BRAF*^{V600E}/*p*Akt/*Trp53*^{KO} tumors (white arrow). Scale bar, 25 µm. Data shown in this figure were modified from Cases-Cunillera et al., 2022.

3.2. *In vivo* growth monitoring of the 1-, 2- and 3-hit tumor models

The results described above demonstrate that the present molecular alterations involving *BRAF*^{V600E}, activation of Akt and *Trp53* knockout lead to a histopathologically distinct tumor model. To determine whether this phenomenon is reflected *in vivo*, the survival data of the different mouse models were collected and further analyzed. A weight loss of 20 % was selected as the main criteria for sacrificing the animals. The analysis of the survival of *BRAF*^{V600E} mice showed that mice survived until P100 without any sign of malignancy (n = 8; **Fig. 8A**). The additional activation of the Akt/mTOR signaling cascade to the BRAF^{V600E} (*BRAF*^{V600E}/*p*Akt) did not worsen the phenotype of these animals and reflected a benign biological behavior (n = 9; **Fig. 8A**). However, in line with the pleomorphic/aberrant histological features shown by *BRAF*^{V600E}/*p*Akt/*Trp53*^{KO}, the addition of a *Trp53* loss did impact the phenotype of the mice with the overall survival rate being at 0 % at the age of P70 (n = 19; **Fig. 8A**). Moreover, the malignant phenotypical profile correlated with the proliferation potential of these tumors, quantified by the percentage of Ki67 immunoreactive cells (**Fig. 8B**). While *BRAF*^{V600E} and *BRAF*^{V600E}/*p*Akt tumors displayed a Ki67 labeling index lower than 5 %, the quantification of Ki67-immunolabeled cells in *BRAF*^{V600E}/*p*Akt/*Trp53*^{KO} tumors revealed a Ki67-based proliferation index of almost 50 % (**Fig. 8C**).

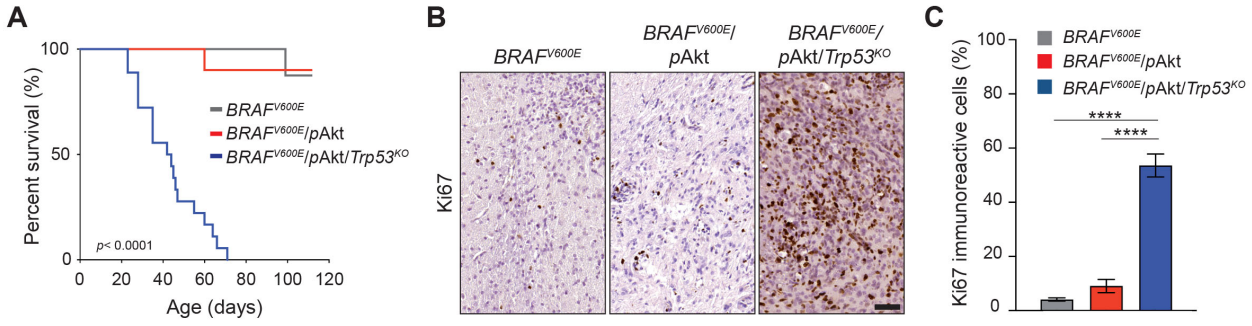

Fig. 8. Survival kinetics of tumor harboring mice and neoplasm intrinsic proliferation. (A) Survival rates of *BRAF*^{V600E}, *BRAF*^{V600E}/*p*Akt and *BRAF*^{V600E}/*p*Akt/*Trp53*^{KO} tumor mice. Kaplan-Meier survival curve showing the survival times of *BRAF*^{V600E}, *BRAF*^{V600E}/*p*Akt and *BRAF*^{V600E}/*p*Akt/*Trp53*^{KO} (P110) tumor mice. Log-rank test, $p < 0.0001$. (B) Representative images of brain sections from the different tumor models stained against the proliferation-related antigen Ki67. Scale bar, 25 µm. (C) Quantification of Ki67 immunoreactive index (n = 3 - 5 different animals with n = 10 micrographs per group). Data are represented as mean ± SEM. One-way ANOVA followed by Tukey´s multiple comparison test, ****$p < 0.0001$. Data shown in this figure contributed to Figure 4 in Cases-Cunillera et al., 2022.

The tumor growth dynamics of the distinct tumor models were then explored to get more information on their growth patterns. While the Ki67 labeling index gives information on the tumor behavior at the last stage, it does not provide data on the growth kinetics over time. Therefore, a plasmid coding for a near-infrared fluorescent protein (iRFP^{713}; (Richie et al., 2017)) was co-IU-electroporated together with the plasmids encoding for the oncogenes to generate tumors harboring an *in vivo* reporter protein. The imaging of the signal from tumor brains expressing iRFP was performed at P10, P20 and P45. Interestingly, *BRAF*^{V600E} and *BRAF*^{V600E}/*p*Akt tumors showed different growing patterns at earlier time points. While iRFP signal did not detect any premature growth of *BRAF*^{V600E} tumor, suggesting exhaustion already at P10 (**Fig. 9A** and **D**), *BRAF*^{V600E}/*p*Akt tumors preserved a growing capability until P20 by showing a significant increase of the iRFP-derived signal compared to P10 (**Fig. 9B,** and **E**). Intriguingly, the iRFP-based signal from *BRAF*^{V600E}/*p*Akt tumors was reduced at P45, which could be reasoned by a possible loss of tumor cells at this time point. This aspect would agree in favor of a lack of growth potential by these tumors.

Finally, the iRFP signal from *BRAF*^{V600E}/*p*Akt/*Trp53*^{KO} tumor cells increased until P45 (**Fig. 9C** and **F**) reflecting its high growth potential.

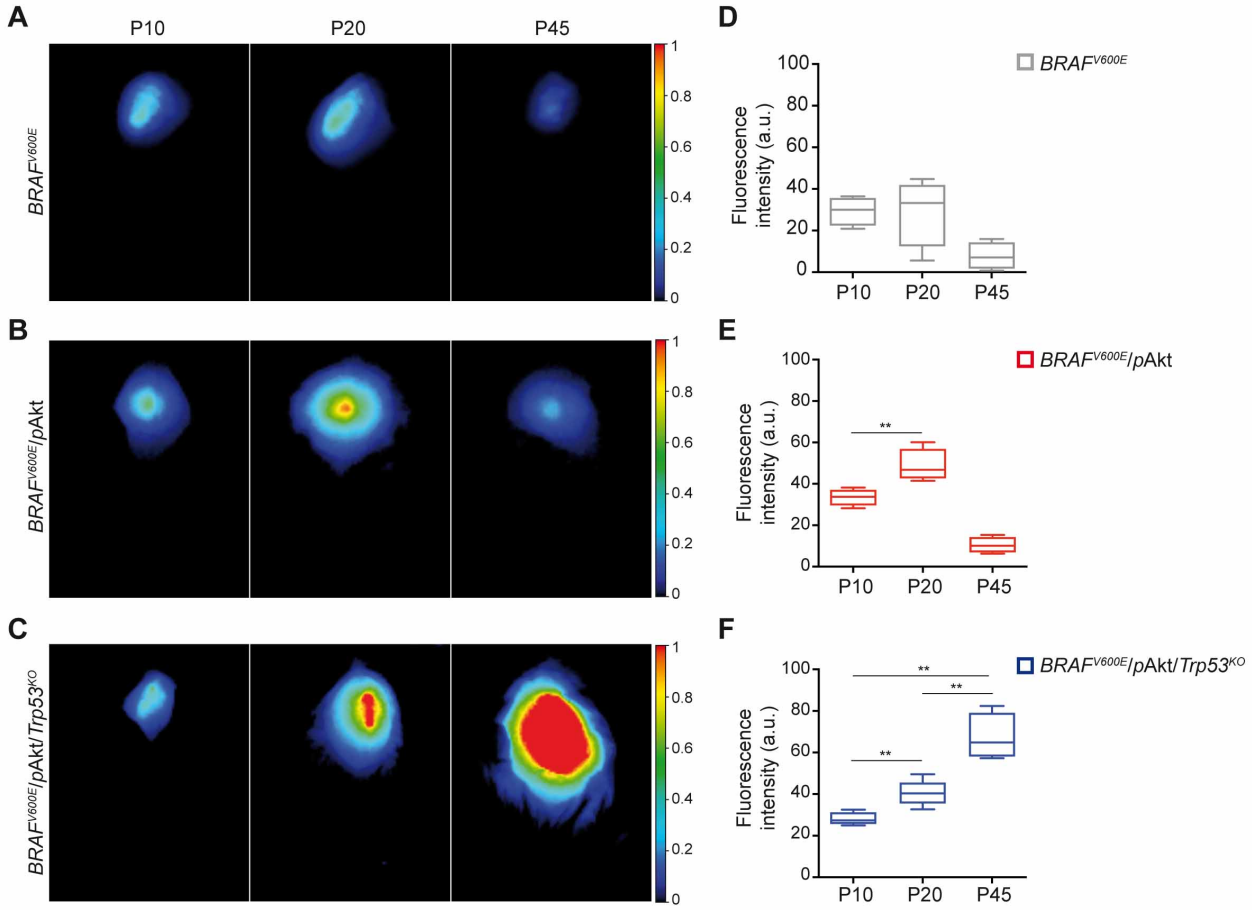

Fig. 9. *In vivo* growth kinetics of murine 1-, 2- and 3-hit tumor models. (A-C) *In vivo* iRFP signal from *BRAF*^{V600E} (A), *BRAF*^{V600E}/*p*Akt (B) and *BRAF*^{V600E}/*p*Akt/*Tp53*^{KO} (C) mouse brains detected at P10, P20, and P45 (color bar - total fluorescence efficiency in pseudo-color). (D-F) Quantification of iRFP signals from the tumor brains. Regions of interest (ROIs) were defined above the tumor region and the fluorescence intensity was defined in arbitrary units (a.u.). One-way ANOVA followed by Tukey´s multiple comparisons test; * $p < 0.05$; ** $p < 0.01$; n = 4 – 6 per group. Data shown in this figure contributed to Figure 4 in Cases-Cunillera et al., 2022.

3.3. Clonality aspects of *BRAF*^{V600E}/*p*Akt/*Trp53*^{KO} tumors analyzed by genetic multicolor fluorescence imaging

The glioneuronal architecture of GGs triggered a discussion about the origin of these neoplasms. It is not fully understood whether they develop (*1*) from a precursor cell with the capability of generating both neuronal and glial components or (*2*) from alterations affecting neurons and glial cells separately. Thus, as an attempt to clarify the nature of these neoplasms, a multicolor reporter was IU-electroporated in the *BRAF*^{V600E}/*p*Akt/*Trp53*^{KO} tumor model. The lineage tracer Brainbow was used as a tool to

study the clonal growing and spread of these neoplasms. Brainbow cassette relies on a Cre/*loxP* stochastic recombination of distinct fluorescent proteins, and it has been shown to specifically label a cell population which develops from the same progenitor with the same fluorescent color combination as their parental cell (Cai et al., 2013; Livet et al., 2007).

First, the Brainbow 3.0 cassette was cloned into the piggyBac vector under the control of the CAG constitute promoter (**Fig. 10A**). To simplify the microscopic visualization of the Brainbow protein-derived colors, the Brainbow-expressing cells were always imaged for green fluorescent protein (GPF) and red fluorescent protein (RFP) expression. The functionality of the Brainbow system was then tested by HEK 297 cell transfection. The single transfection of the Brainbow plasmid in HEK 297 cells exclusively led to GFP-labeled cells, while the co-transfection with the Cre transposase elicited the additional presence of RFP-positive cells (**Fig. 10B**). Moreover, Brainbow-expressing plasmid was also IU-electroporated in mice at E14 and the further analysis of the brain sections confirmed the multicolor labeling upon Cre injection (**Fig. 10C**).

After verifying the functionality of the plasmid, the Brainbow system was applied to the *BRAF*^{V600E}/*p*Akt/*Trp53*^{KO} animal model. For this purpose, the Brainbow construct was co-IU-electroporated together with the oncogenes. To assess the fluorescence derived from the Brainbow proteins, the sequence encoding for mCherry protein was removed from the oncogene plasmids (**Fig. 10A**). The analysis of the resulting brains (E21) showed the presence of distinct clones labeled in distinct fluorescent colors. Some groups of tumor cells expressed only RFP or GFP, but cell populations expressing a mixture of both fluorescent proteins were also present (**Fig. 11A**), probably as a result of the fast clonal expansion of the tumor. The glioneuronal assessment in one specific clone was done with staining against GFAP (glial-specific) and NeuN (neuronal-specific) markers. The results showed that cells immunolabeled either with GFAP or NeuN were present within the same brainbow-derived clone (**Fig. 11B**), leading to the conclusion that these tumors can grow in a clonal manner from one single precursor cell giving rise to dysmorphic neurons and neoplastic astrocytes.

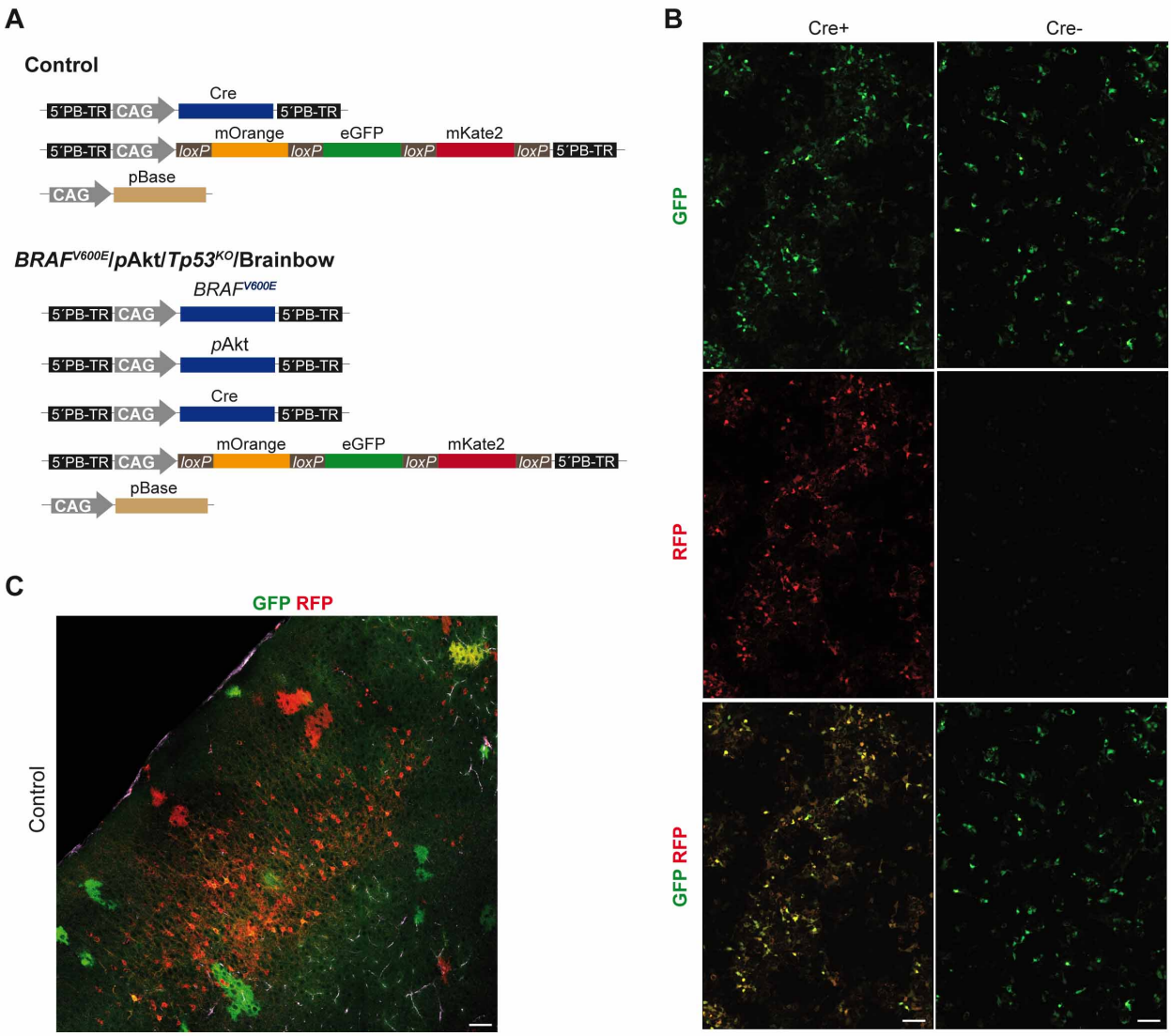

Fig. 10. Brainbow-derived fluorescent assessment with and without the presence of Cre transposase expression. (A) Schematic diagram of the DNA constructs encoding the Brainbow system for Control and *BRAF*^{V600E}/*p*Akt/*Trp53*^{KO}. (B) Images from HEK 287 cells transfected with the Brainbow cassette with and without Cre transfection. While the transfection of Brainbow alone leads to the presence of only GFP-labeled cells, upon Cre transfection both GFP- and RFP-labeled cells are visualized. Scare bar, 100 µm. (C) Overview of the cortical area at P20 of a mouse brain IU-electroporated at E14 with Brainbow and Cre. Note that the presence of Cre allows the stochastic recombination of the fluorescent proteins leading to different color-labeled clones. Scale bar, 100 µm. Data shown in this figure were modified from Cases-Cunillera et al., 2022.

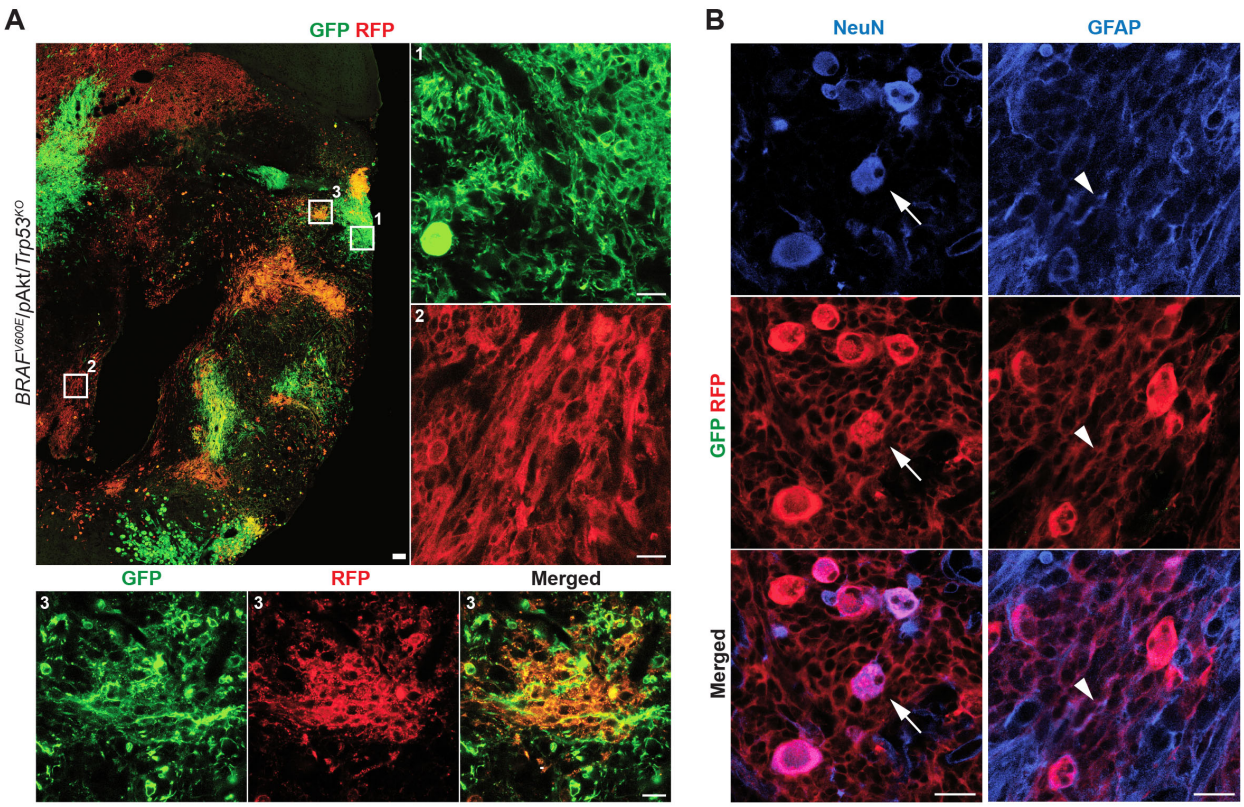

Fig. 11. Images from *BRAF*^{V600E}/*p*Akt/*Trp53*^{KO} tumors expressing Brainbow multicolor tracer. (A) *BRAF*^{V600E}/*p*Akt/*Trp53*^{KO} brain sections expressing the fluorescent proteins derived from the Brainbow construct (n = 5). Note the presence of different clones visualized by the GFP and RFP channels. Overview of a representative tumor brain slice (left panel; scale bar, 100 µm). Higher magnification images from the left panel (white squares) of the corresponding clones positive for GFP (1), RFP (2) and a combination of both colors (3) (right and lower panels; scale bar, 25 µm). (B) Stainings against NeuN and GFAP of *BRAF*^{V600E}/*p*Akt/*Trp53*^{KO}/Brainbow brain slices within a clone positive for RFP. Scale bars, 25 µm. Data shown in this figure contributed to Figure 3 in Cases-Cunillera et al., 2022.

3.4. Excitability aspects of the GG mouse models

3.4.1. Quantification of extracellular activity from acute brain slices in a spatial-dependent manner

Multielectrode array (MEA) enables the recording of extracellular activity. Even though it was designed for neuronal cultures, its application has been translated also to human and murine brain slices (Dossi et al., 2014; Reinartz et al., 2014). For the application of this technical approach, the neuronal activity was assessed in a location-dependent manner from control, *BRAF*^{V600E}, *BRAF*^{V600E}/*p*Akt and *BRAF*^{V600E}/*p*Akt/*Trp53*^{KO} brain sections (n

= 7 – 21, from 3 to 6 mouse brains per group). Acute brain slices (300 µm) were placed onto a 64-electrode grid in a MEA plate with either artificial cerebrospinal fluid (aCSF) or with a solution favoring network activity (aCSF with low $Mg^{2+,}$ high K^{+}). The region of the tumor was visualized and imaged on the electrodes by the fluorescent signal in order to subsequently correlate it with the neuronal activity. As a control, the same experimental approach was applied to brains expressing mCherry alone. Each electrode was classified according to the distribution of the fluorescent tissue into three categories: (*1*) IUE Tumor core (area with mCherry-positive tumor cells), (*2*) Peri-IUE (tumor border) and (*3*) Non-fluorescent tissue (pre-existing brain tissue; **Fig. 12A**). Tumor slices were stained with HE to prove that the presence of the fluorescent signal corresponded to the location of the tumor lesion (**Fig. 12B**). The extracellular activity of the brain slices was recorded from 64 different positions (**Fig. 12C**) for 15 min and the number of spikes were quantified per electrode for each category.

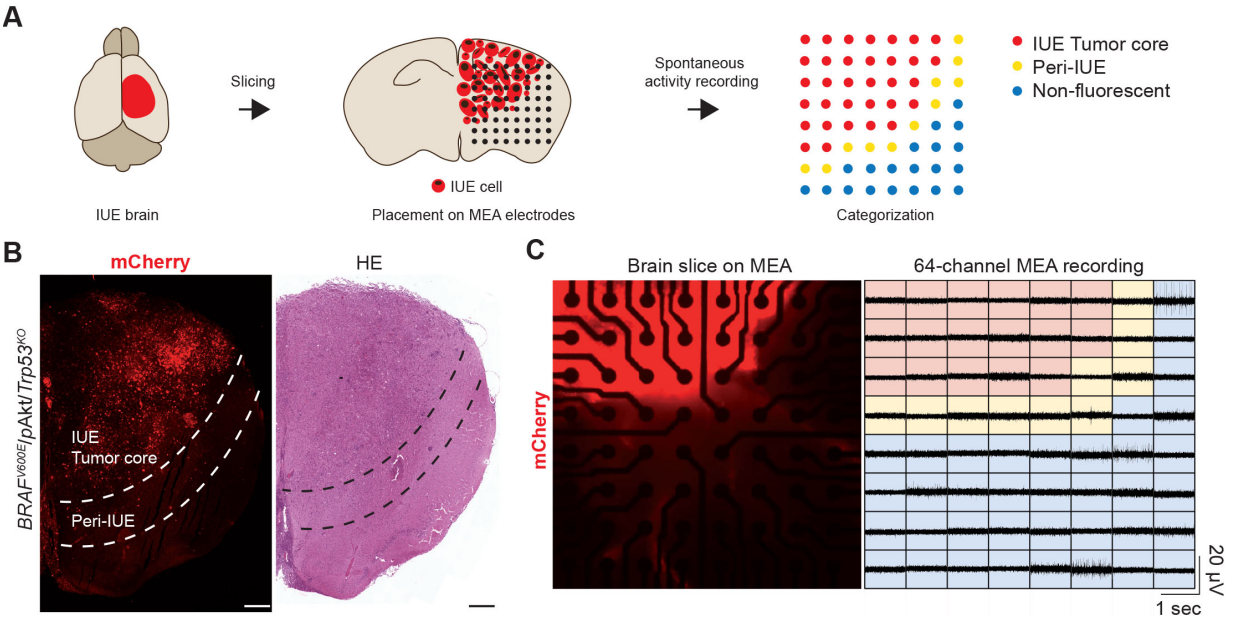

Fig. 12. Spontaneous neuronal activity from murine GG brain slices with MEA system. (A) Schematic diagram depicting the workflow used for MEA recording from acute brain slices. After isolating the mouse brain, the brain slices were cut to 300 µm and placed onto the 64-electrode grid in the MEA plate by visualizing the fluorescent signal. Neuronal spontaneous activity was recorded for 15 min. The electrodes were further classified into (1) IUE Tumor core (electrodes interacting with tissue expressing fluorescent protein), (2) Peri-IUE (electrodes in contact with tissue adjacent to fluorescent signal) and (3) Non-Fluorescent (electrodes in contact with tissue without any fluorescence expression). (B) Overview image of a tumor brain slice expressing fluorescent signal (left panel). White stripe lines show the borders of the regions defining the three categories. The right panel shows the corresponding HE-stained section. Scale bar, 500 µm. (C)

Representative fluorescent signal from a tumor brain slice located on the MEA grid consisting of 64 electrodes (left panel). Extracellular voltage signal traces were recorded by each of the electrodes highlighted according to their category (right panel). Data shown in this figure contributed to Figure 6 in Cases-Cunillera et al., 2022.

3.4.2. Inter-model differences in neural spontaneous activity across different developmental brain tumors harboring *BRAF*^{V600E}

The analysis of the average number of spikes per electrode from brain slices incubated in aCSF showed that while the control slices exhibited a homogenous firing non-dependent on the category, the electrical activity of tumor slices showed differences among categories (**Fig. 13A**). Since the resulting spike traces of tumor slices showed the same pattern as the control (**Fig. 13B**), we rule out the notion of potential interference in the neural activity firing from the tumor lesion.

Some similarities among the tumor models were observed with the tumor core being the most silenced region for all induced neoplasms compared to the peri-tumoral and surrounding tissue (**Fig. 13C**). Moreover, the frequency of the neuronal activity in the peri-tumoral and surrounding tissue was equivalent to the control levels for all tumor groups (**Fig. 13C**). However, differences between tumor variants were identified regarding the contribution to the number of spikes by each category. While *BRAF*^{V600E} and *BRAF*^{V600E}/*p*Akt/*Trp53*^{KO} tumor core-derived neuronal activity was almost absent and differed significantly in the number of spikes/electrode from the control group, no significant change was detected between the tumor core of *BRAF*^{V600E}/*p*Akt and control groups (**Fig. 13C**).

In parallel, the same analysis was performed after potentiating the neuronal activity of brain slices with aCSF solution with low Mg^{2+} and high K^{+}. Interestingly, only the activity from the control IUE core region could be increased, without the possibility to potentiate the neural activity for any of the tumor cores (**Fig. 13D**). Interestingly, in the peri-tumoral area only the neuronal activity of *BRAF*^{V600E}/*p*Akt neoplasms could be potentiated, in contrast to *BRAF*^{V600E} and *BRAF*^{V600E}/*p*Akt/*Trp53*^{KO} peri-tumoral regions, which appeared to remain almost silenced. A potentiation within the non-IUE tissue was observed for all the tumor models indistinctly from control (**Fig. 13D**).

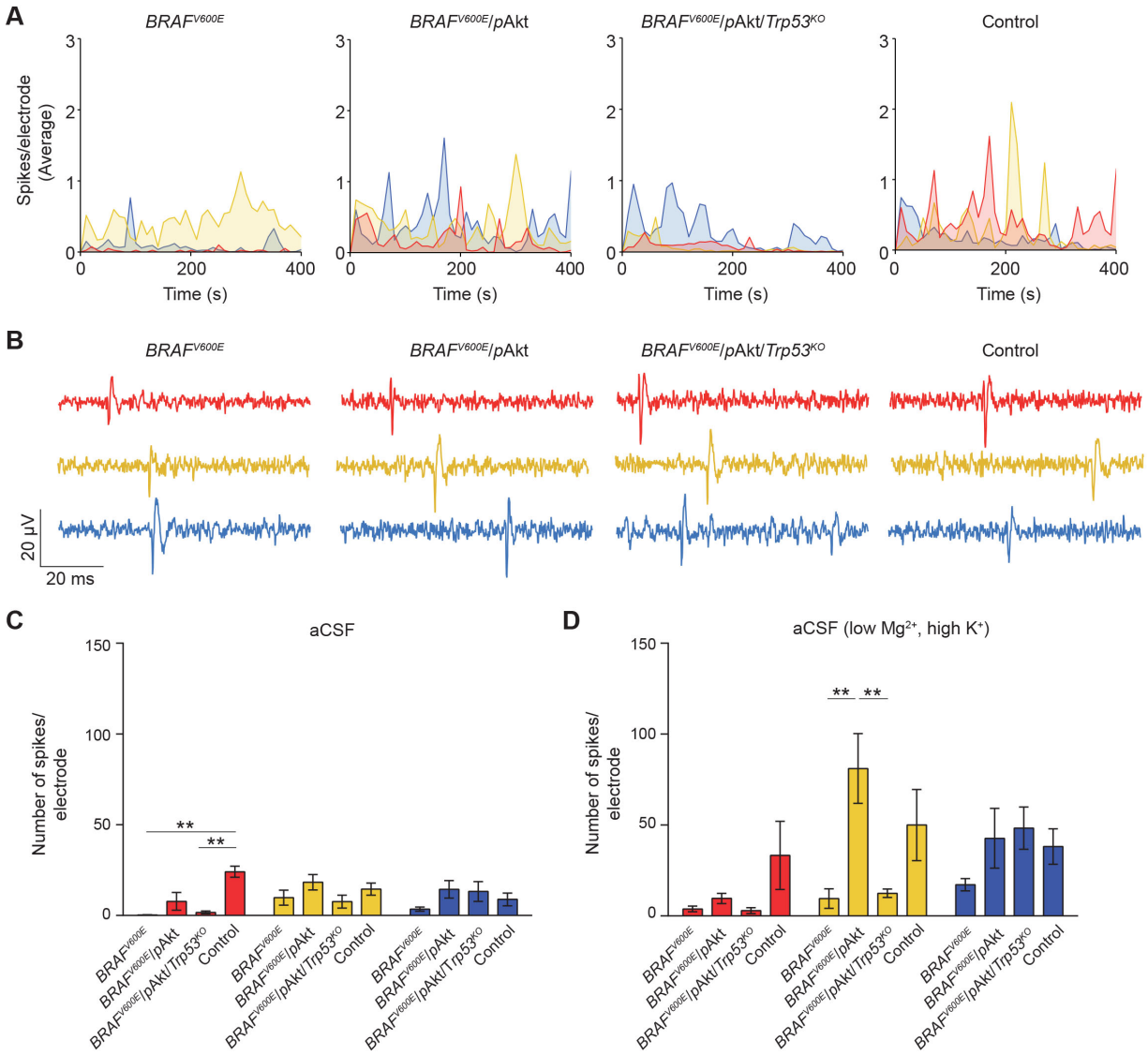

Fig. 13. Category-dependent inter-model comparison of the number of spikes/electrode. (A) Average of the number of spikes/electrode over time for *BRAF*^{V600E} (n = 7), *BRAF*^{V600E}/*p*Akt (n = 21), *BRAF*^{V600E}/*p*Akt/*Tp53*^{KO} (n = 21) and control (n = 14) brain slices colored according to category (*red* for IUE Tumor core; *yellow* for peri-IUE and *blue* for Non-fluorescent). Spontaneous neural activity was measured for 15 min from slices incubated in aCSF. Time bin = 10 sec. Biological replicates; 3 – 6 mice per group. (B) Representative traces of spontaneous neuronal activity of slices incubated in aCSF (80 µsec) for each tumor group and control and for all categories. Of note, the spikes from tumoral slices have the same pattern as the control. (C) Bar graph showing the inter-model comparison of the total number of spikes per electrode averaged for all slices incubated in aCSF during 15 min. While the neuronal activity of the *BRAF*^{V600E} and *BRAF*^{V600E}/*p*Akt/*Tp53*^{KO} tumor cores appeared significantly reduced compared to control, *BRAF*^{V600E}/*p*Akt did not show a statistical change. (D) Quantification of the averaged number of spikes/electrode from tumor and control brain slices incubated with aCSF (low Mg^{2+}, high K^{+}). Of note, high increase in neuronal activity for *BRAF*^{V600E}/*p*Akt and control compared to *BRAF*^{V600E} and *BRAF*^{V600E}/*p*Akt/*Tp53*^{KO} groups. Data are represented as mean ± SEM. One-way ANOVA was

followed by Tukey´s multiple comparison test. **p < 0.01. Data shown in this figure contributed to Figure 6 in Cases-Cunillera et al., 2022.

3.5. Comprehensive transcriptomic analysis of *BRAF*^{V600E}/*p*Akt- and *BRAF*^{V600E}/*p*Akt/*Tp53*^{KO}-induced tumors

The following work section focuses on the expression profiles in *BRAF*^{V600E}/*p*Akt and *BRAF*^{V600E}/*p*Akt/*Tp53*^{KO} tumors by bulk RNA sequencing (RNA-seq). The tumor tissue was compared to respective control tissue matched for grey and white matter dissociated from the same mouse brains. Out of 294 DEGs in *BRAF*^{V600E}/*p*Akt compared to control (n = 4 per group; P110; **Fig. 14A**), 290 genes were found to be upregulated. Of note, in line with the neoplastic features shown by the astrocytes in this tumor model, *Gfap* mRNA was highly abundant in the tumors. The RNA-seq analysis of gene expression between *BRAF*^{V600E}/*p*Akt/*Tp53*^{KO} tumors and corresponding controls (n = 4 per group; P40; **Fig. 14B**) identified a high number of genes to be differentially expressed (3141 genes were augmented and 2700 genes were reduced).

Furthermore, in line with the fact that both tumor models share histological features characteristic of human GGs, in *BRAF*^{V600E}/*p*Akt and *BRAF*^{V600E}/*p*Akt/*Tp53*^{KO} tumors, 255 genes were found to overlap in both samples and only 39 differentially expressed genes were unique for *BRAF*^{V600E}/*p*Akt tumors (**Fig. 14C**). As shown before, both tumors have a distinct biological behavior. Concomitantly, the principal component analysis (PCA) of the RNA-seq data revealed a clear transcriptomic separation according to the underlying genetic alterations (**Fig. 14D**).

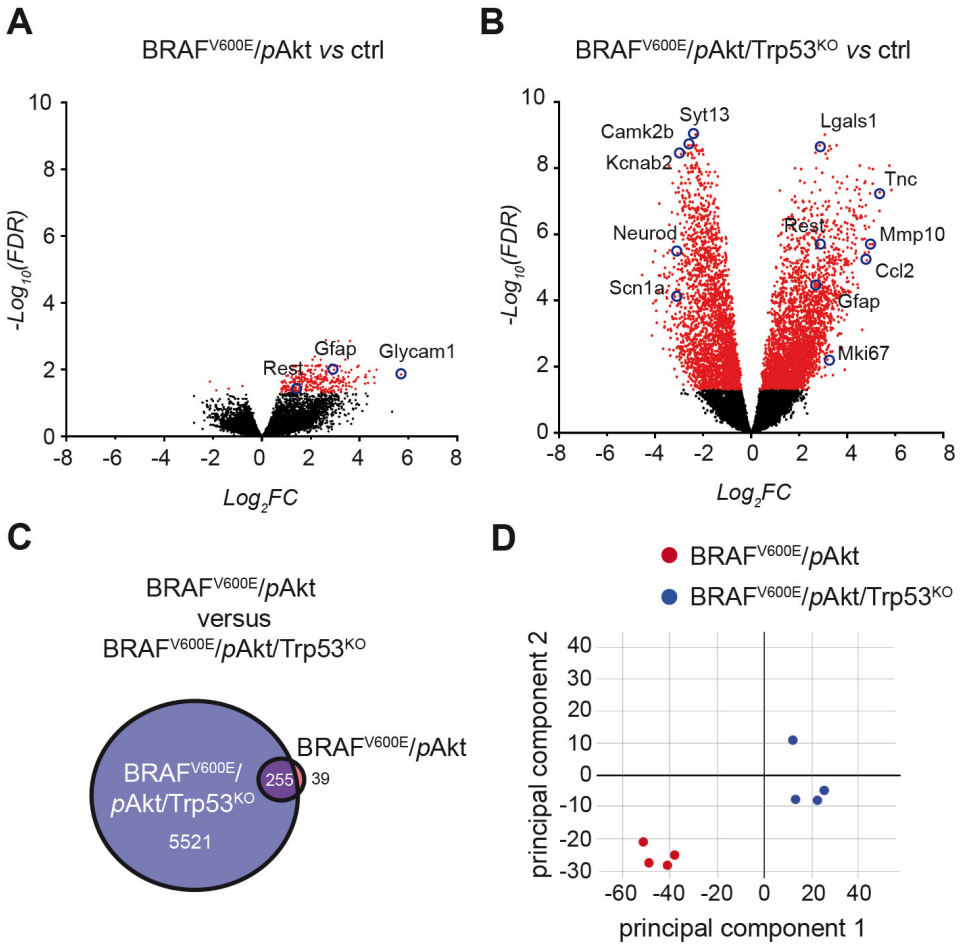

Fig. 14. Transcriptomic assessment of *BRAF*^{V600E} and *BRAF*^{V600E}/pAkt tumor tissue with bulk RNA sequencing. (A, B) Volcano plot representation of the gene expression levels according to $\log_2$ fold change (Log_2FC; x-axis) and adjusted p-value (False Discovery Rate, FDR; y-axis) for (A) *BRAF*^{V600E}/pAkt and (B) *BRAF*^{V600E}/pAkt/*Tp53*^{KO}. Of note, *BRAF*^{V600E}/pAkt tumor tissue shows a lower number of differentially expressed genes (n = 294) compared to *BRAF*^{V600E}/pAkt/*Tp53*^{KO} (n = 5776). The differential gene expression between tumor and control tissue (ctrl) was analyzed from the same brain. Each dot represents one gene colored according to the FDR; in *red*, differentially expressed genes (DEGs; FDR < 0.05) and in *black*, genes that are not differentially expressed (FDR > 0.05). *Blue* circles indicate a selection of significantly increased or decreased genes playing an important role in the process of tumorigenesis. (C) Venn diagram representation displays the DEGs shared between *BRAF*^{V600E}/pAkt and *BRAF*^{V600E}/pAkt/*Tp53*^{KO}. Note the high proportion of DEGs (255 out of 294) in *BRAF*^{V600E}/pAkt overlapping with *BRAF*^{V600E}/pAkt/*Tp53*^{KO}. (D) Principal component analysis (PCA) visualization distinguishes *BRAF*^{V600E}/pAkt and *BRAF*^{V600E}/pAkt/*Tp53*^{KO} tumor samples from each other. Data shown in this figure were modified from Cases-Cunillera et al., 2022.

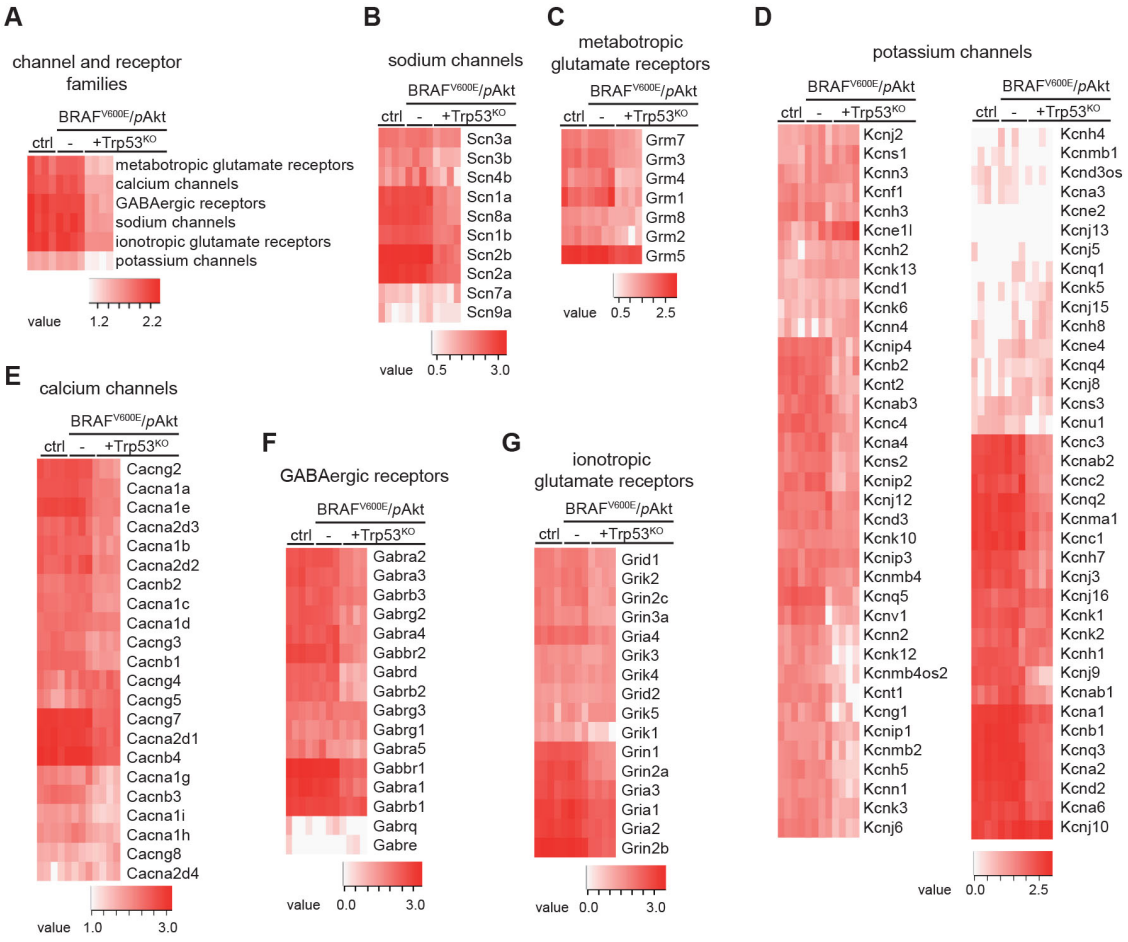

Fig. 15. Differential expresison of synaptic-related receptors and channels in *BRAF*^{V600E}/pAkt/*Tp53*^{KO}, compared to *BRAF*^{V600E}/pAkt and control. Heatmap visualizations of expression levels of genes coding for sodium channels (B), metabotropic glutamate receptors (C), potassium channels (D), calcium channels (E), GABAergic receptors (F), ionotropic glutamate receptors (G) and potassium channels (H) in control (ctrl), *BRAF*^{V600E}/pAkt and *BRAF*^{V600E}/pAkt/*Tp53*^{KO} groups. Each row represents the mean of FPKM values for a group of genes (A) or the individual genes (B-G). Gene expression level is color-coded from *light red* (low expression) to *dark red* (high expression).

Next, the levels of expression of synaptic-related genes were assessed and further classified into channel and receptor families (metabotropic glutamate receptors, calcium channels, GABAergic receptors, sodium channels, ionotropic glutamate receptors and potassium channels). The subsequent results showed that the levels of a high number of channels and receptors were reduced in *BRAF*^{V600E}/pAkt/*Trp53*^{KO}, compared to *BRAF*^{V600E}/pAkt and control (**Fig. 15A**). In line with a more active neuronal network within the *BRAF*^{V600E}/pAkt tumor, most of the genes showed more similar expression levels to control. The analysis of the individual gene expression for each ion channel and

neurotransmitter receptor transcripts showed some sets of genes being reduced in *BRAF*^{V600E}/*p*Akt/*Trp53*^{KO} while other genes remain unchanged, compared to *BRAF*^{V600E}/*p*Akt and control (**Fig. 15B-G**). *BRAF*^{V600E}/*p*Akt tumors showed a 'synapse-related' transcriptomic signature with higher similarity levels to control brain tissue compared to *BRAF*^{V600E}/*p*Akt/*Trp53*^{KO} tumors.

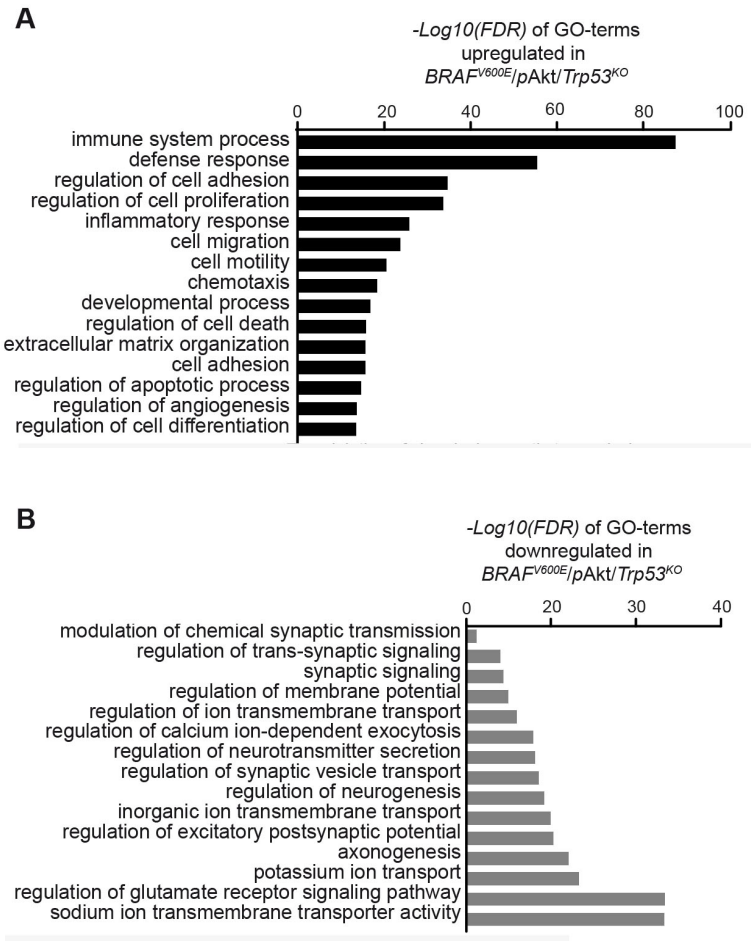

Fig. 16. Gene Ontology (GO) terms from differentially expressed genes in *BRAF*^{V600E}/*p*Akt/*Trp53*^{KO} compared to control. GO terms of the upregulated (A) and downregulated (B) genes in *BRAF*^{V600E}/*p*Akt/*Trp53*^{KO}, compared to control cells. Differential gene expression was defined by FDR < 0.05.

The high number of differential expressed genes reflects the more undifferentiated cellular phenotype of *BRAF*^{V600E}/*p*Akt/*Tp53*^{KO} tumors compared to control tissue. To obtain detailed insights into the expression profile of these tumors a subsequent gene ontology (GO) analysis was carried out. Whereas transcripts with a strong expression in *BRAF*^{V600E}/*p*Akt/*Tp53*^{KO} tumor tissue were related to (innate) immune processes,

proliferation and migration (**Fig. 16A**), reflecting the involvement of astroglial and microglial cells, gene transcripts with functional roles in synaptic signaling and plasticity, neurotransmission and ion-flux were strongly reduced in *BRAF*^{V600E}/*p*Akt/*Tp53*^{KO} tumor tissue (**Fig. 16B**).

3.6. Immunohistochemical analysis of microglia cells in 2-, and 3-hit mouse GGs

The results of the RNA-seq experiments point to a robust level of immunological activation in the analyzed tumors that may resemble microglial cells. In order to determine more in detail the cells conferring the relevant expression signatures, immunohistochemical analyses were conducted next.

Immunohistochemical staining against the microglial-specific marker Iba1 showed a very strong labeling reaction within the tumor region of both *BRAF*^{V600E}/*p*Akt and *BRAF*^{V600E}/*p*Akt/*Trp53*^{KO} tumors (**Fig. 17**), compared to control, leading to the conclusion that both these tumors are very immunogenic. Of note, the microglial cell component was very heterogeneous regarding its morphology and size, suggesting that distinct states of activation and differentiation are present within the same immune cell type.

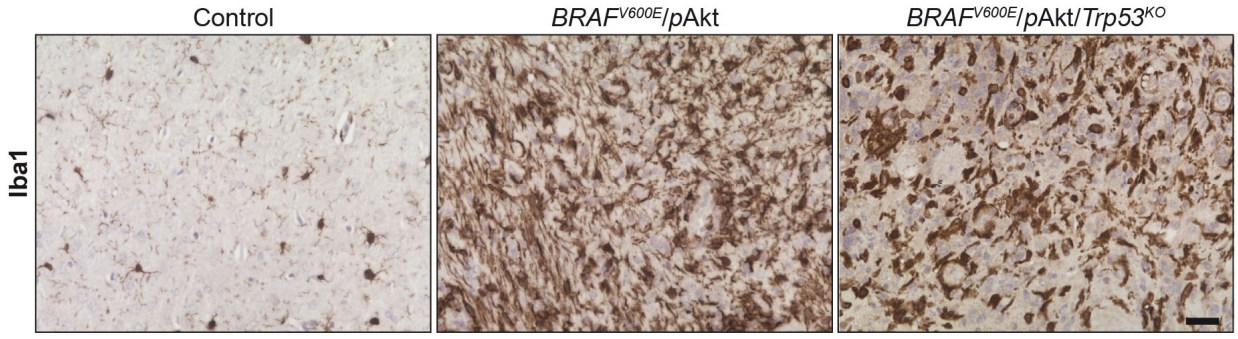

Fig. 17. Representative images from Iba1-stained brain sections. Images from control, *BRAF*^{V600E}/*p*Akt and *BRAF*^{V600E}/pAkt/*Tp53*^{KO} stained against Iba1, a microglia-specific marker. Scale bar, 25 µm.

4. Discussion

The present study has applied *in vivo* model approaches in order to test systematically the role of *BRAF*^{V600E}, so far only descriptively reported in human epilepsy associated tumors including GGs (Chappé et al., 2013; Dougherty et al., 2010; Schindler et al., 2011) and PLNTYs (Huse et al., 2017) in concert with additional key molecular alterations reported in human epilepsy associated tumor biopsies and of unresolved pathological significance. The newly generated developmental tumor models were further applied for gaining novel insights into the detailed cellular composition and the functional states of cell components as well as phenotypic characteristics, by which the different emerging neoplasms manifest, and the interplay of the tumor and peritumoral compartments with respect to excitability.

4.1. *BRAF*^{V600E} acts cellular and molecular context-dependent in developmental brain tumorigenesis

The present data demonstrated that *BRAF*^{V600E} expressed together with *p*Akt at E14 resulted in adult mouse tumors that recapitulated strikingly characteristic neuropathological features of human GGs. In contrast, Koh and colleagues claimed that the expression of *BRAF*^{V637E} (the murine equivalent of *BRAF*^{V600E}) during embryonic stages was sufficient for the emergence of glioneuronal neoplasms with GG features. In our present study, neoplasms that were induced only with *BRAF*^{V600E} resembled neuropathological features of a minority of GGs, mostly characterized by irregularly oriented but not largely dysmorphic neurons and a rather neurocytic than true glial neoplastic component. These tumors were within the neuropathological spectrum, but they resembled the characteristic oligoid features of PLNTYs in adult mice.

This discrepancy may be due to the fact that Koh and colleagues used the murine equivalent *BRAF*^{V637E} to induce tumors. The true effect of both mutant variants may not be strain-specific but may have slightly different activating effects which may explain part of the discrepancy. However, they also described rather aberrantly shaped than true dysmorphic neurons. This is in line with results presented in this study showing that expression of *BRAF*^{V600E} alone triggered neoplasms lacking dysmorphic neuronal cells.

Another reason for these contradictory findings could rely on the particular modalities of induction of mutant *BRAF* in embryonal mouse brains. Koh and colleagues used IUE of a plasmid encoding for Cre transposase in a mouse model that carried *Braf* knock-in allele, leading to the production of the V637E mutant BRAF protein. In the present study, DNA carrying $BRAF^{V600E}$ is injected directly into the neural precursors and does not depend on the protein production of the Cre transposase. Therefore, the effect of the mutated BRAF-variant may manifest within a slightly different developmental time-window than occur in the present model leading to substantial consequences on the resulting tumors.

In fact, the cellular architecture and the biological behavior of brain tumors induced in mice based on $BRAF^{V600E}$ may be strongly dependent on the targeted neural cell population and the induction protocol. *In vivo* retroviral somatic gene transfer into neonatal mouse neural cells demonstrated that ectopic expression of the activated BRAF kinase domain was sufficient to induce pilocytic astrocytomas in mice (**Table 4**, (Gronych et al., 2011)). Another study demonstrated that $BRAF^{V600E}$ expression during embryonic stages under the control of GLAST or Nestin promoters triggered glioneuronal tumors with somewhat different neuropathological features compared to tumors arising from our reported experimental strategy (**Table 4**, (Goz et al., 2020)). Furthermore, Robinson and colleagues showed that viral inoculation of activated BRAF alone into the brain of newborn mice induced tumorigenesis. However, in combination with an activated Akt variant, tumors harboring $BRAF^{V600E}$ were highly pleomorphic, and contained a large spectrum of cells with different morphology recapitulating features of glioblastoma multiforme (GBM; **Table 4**, (Robinson et al., 2010)). Intriguingly, the present data suggested that $BRAF^{V600E}$ together with *p*Akt introduced into neural precursor populations at E14 with IUE generated benign neoplasms most closely resembling GGs. Thus, the distinct cell population subjected to activated MAPK and Akt/mTOR signaling is critical for both, neuropathological appearance and malignancy of the emerging tumors. The outlined data may be in line with the concept that the more differentiated the cells hit by $BRAF^{V600E}$ the less benign the developing neoplasms are.

Table 4. Overview of existing animal models for *BRAF*^{V600E} -positive tumors. Summary of tumor characteristics and biological behavior of murine tumor models triggered by IUE by distinct oncogene combination involving *BRAF*^{V600E}, *p*Akt and *Trp53*-loss (first half of the table). Overview of existing current literature related to animal models triggered by the expression of *BRAF*^{V600E} (second half of the table). Data shown in this figure contributed to Supplementary Table 1 in Cases-Cunillera et al., 2022.

Mouse model	Genetic manipulation/promoter	Tumorigenicity	Glial cell fraction	Neuronal cell fraction	Biological behavior	Corresponding human tumor entity / major neuropathology/
***BRAF*^{V600E}**	*IUE (CAG-promoter); pB-TP*[a]	+	*oligoid*	-	*benign*	*PLNTY*
***p*Akt**	*IUE (CAG-promoter); pB-TP*	-				
***Trp53*^{KO}**	*IUE (CAG-promoter); pB-TP*	-				
***BRAF*^{V600E} /**	*IUE (CAG-promoter); pB-TP*	+	*astroglial*	*dysmorphic*	*benign*	*GG (WHO grade I)*
***BRAF*^{V600E} /**	*IUE (CAG-promoter); pB-TP*	-	*astroglial*	*dysmorphic*	*malignant*	*anaplastic GG (WHO grade III)*

Glast-	*IUE (GLAST-promoter); pB-TP*		*Astrocyto-genesis,* *balloon cells*	*mislocated*	*benign*	(Goz et al., 2020)
Nestin-	*IUE (NESTIN-promoter); pB-TP*		*balloon cells*	*mislocated,* *enlarged soma*	*benign*	(Goz et al., 2020)
LSL[b]-BRAF$^{V637E/+}$	*IUE episomal pCAG-Cre*		*Increased number of astro- or oligoden-drocytes*	*dysmorphic, dyslamination*	*benign*	*similarity to GG* (Koh et al., 2018)
BRAF^{V600E} KinD[c]	*NESTIN-promoter, retroviral vector; neonatal Ntv mice*	+	*piloid*	-	*benign*	*pilocytic astrocytom a* (Gronych et al., 2011)
BRAF^{V600E}/act.	*retroviral vector; neonatal Ntv mice*		*pleomorphic, including 'giant cells'*	-	*malignant*	*GBM* (Robinson et al., 2010)

[a]pB-TP - piggyBac transposon system.

[b]LSL - *LoxP*-stop-*LoxP* (Koh et al., 2018)

[c]KinD – kinase domain (Robinson et al., 2010)

[d]activated (act.)Akt - Akt-Myr

As pointed above, our data showed that the ectopic expression of *BRAF*^{V600E} alone in paraventricular neural precursors induced neoplasms with histological features of human PLNTYs. Huse and colleagues reported the term “polymorphous low-grade neuroepithelial tumor of the young” (PLNTY) for the first time in 2017 and it refered to a subgroup of epileptogenic developmental brain tumors mainly characterized by an oligodendroglioma-like cellular composition, alterations affecting *BRAF* and CD34 immunoreactivity (Huse et al., 2017). Immunohistochemically, mouse tumors induced with only *BRAF*^{V600E} resembled the oligoid-like features characteristics of human PLNTYs. The activation status of the Akt/mTOR pathway in human PLNTYs has not been examined in detail. The lack of *p*S6 in distinct human PLNTYs positive for *BRAF*^{V600E} was verified with immunohistochemistry in the present study. Moreover, as concluded by previous reports and our cases, strong immunoreactivity for CD34 is a striking hallmark observed in human PLNTYs. In fact, *BRAF*^{V600E} -induced neoplasms showed a strong immunopositivity for CD34 (data not shown).

These data underline the role of PI3K-pathway activation as a significant modulatory alteration for the effects of *BRAF*^{V600E} on developmental brain tumorigenesis.

4.2. The functional role of mTOR pathway activation in *BRAF*^{V600E}-positive brain tumors

Based on the present observations, *BRAF*^{V600E} alone harbored the potential of triggering neoplasia in mice, but the resulting tumors lacked dysmorphic neuronal elements. *p*S6 expression has been described in human *BRAF*^{V600E} positive GGs (Prabowo et al., 2014). Concomitantly, higher activation of the mTOR signaling pathway has been reported in a larger percentage of neurons in GGs compared to control tissue (Boer et al., 2010). Moreover, synchronous activation of the MAPK cascade protein ERK1/2 together with Akt led to potentiation of mTOR activation in GG cells (Rak et al., 2013).

Aspects of the crosstalk between MAPK and mTOR signaling pathways in the pathogenesis of low-grade tumors have been previously investigated. In fact, activation of the mTOR pathway has been examined in the context of pediatric sporadic gliomas harboring activated BRAF fusion protein (referred to as KIAA1549:BRAF). Kaul and colleagues showed that fusion BRAF triggers S6 phosphorylation in neural stem cells. Moreover, they found mTOR hyperactivation in human tissue samples from pilocytic

astrocytomas positive for KIAA1549:BRAF mutation (Kaul et al., 2012). The present data implied that PI3K-pathway activation in combination with *BRAF*^{V600E} in neural precursors is a key precondition for the emergence of dysmorphic neurons. On a molecular level, *in vitro* analyses confirmed that neural cells co-transfected with *BRAF*^{V600E} and *p*Akt, but not *BRAF*^{V600E} alone, had a significant increase in S6 phosphorylation levels. Intriguingly, neither *BRAF*^{V600E} nor *BRAF*^{V600E}/*p*Akt expression triggered phosphorylation/activation of the downstream protein 4E-BP1 (**Fig. 18**).

As further evidence of the crosstalk between both signaling pathways, Roux and colleagues described an mTOR-independent activation of S6 via the MAPK signaling pathway. While the mTOR downstream protein ribosomal S6 kinase (S6K) could phosphorylate S6 at both S235/6 and S240/4 residues, the ERK1/2 downstream protein ribosomal S6 kinase (RSK) exclusively phosphorylated S6 at S235/6 (Roux et al., 2007). In the present study, the activation of S6 was functionally assessed at both sites leading to the result that expression of *p*Akt was required in combination with *BRAF*^{V600E} to trigger phosphorylation at both residues (**Fig. 18**). Indeed, both sites were found to be phosphorylated in human GGs positive for *BRAF*^{V600E} (Prabowo et al., 2014). Thus, in the present system *BRAF*^{V600E} alone lacked the potential of activating S6. This is in accordance with the data published by Koh and colleagues showing that developmental brain tumor models positive for mutant BRAF did not show increased levels of S6 phosphorylation (Koh et al., 2018).

In fact, high levels of *p*S6 levels at both S235/6 and S240/4 residues were detected in maturing neurons with cytomegaly and dendrite hypertrophy (Iffland et al., 2018; Sokolov et al., 2018). Of note, Sokolov and colleagues demonstrated that the cell growth of cortical neurons and augmented dendritic complexity was mediated by IUE-mediated overexpression of Rheb, which is an activator of mTOR pathway and is regulated by Akt protein. This increase in mTOR pathway was observed together with phosphorylation of S6 (Sokolov et al., 2018). Other reports showed that an increase of *p*S6 phosphorylation triggered by Rheb-dependent mTOR activation led to neurogenesis defects and abnormal synaptic function (Hsieh et al., 2016; Lafourcade et al., 2013).

Together with the present results, these data highlight the influence of the PI3K/Akt/mTOR pathway activation via phosphorylation of S6 protein on the regulation of neuronal phenotype during development

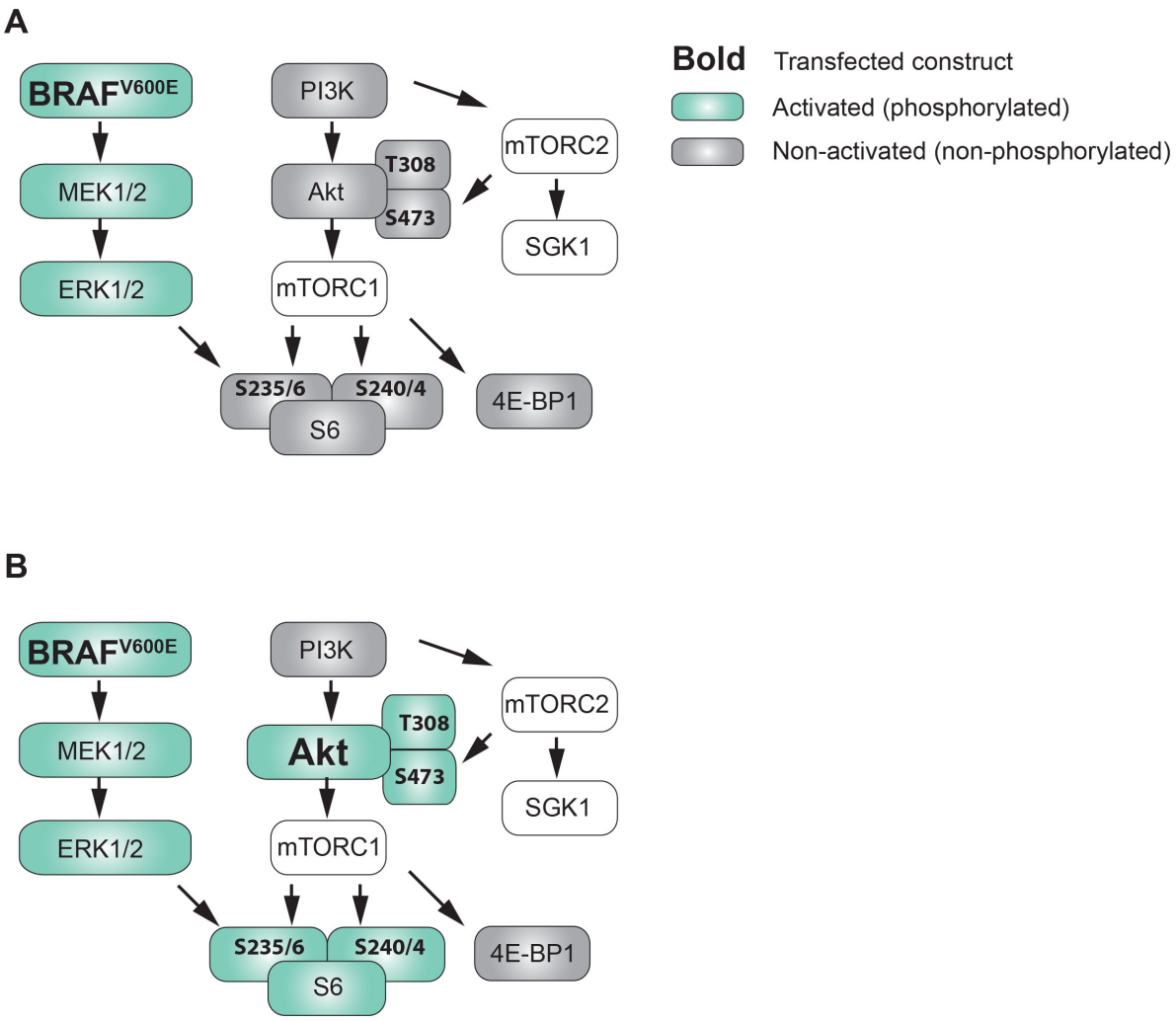

Fig. 18. Summary of functional crosstalk between MAPK and Akt/mTOR signaling pathways in neuronal cells transfected with either *BRAF*^{V600E} or *BRAF*^{V600E}/*p*Akt of data from results section 3.1.1. (A) Transfection of *BRAF*^{V600E} triggers activation of MEK1/2 and ERK1/2 *in vitro*. (B) Neuronal cells co-transfected with *BRAF*^{V600E} and *p*Akt show high S6 phosphorylation levels at S235/6 and S240/4. Activated/phosphorylated proteins are depicted in green. Non-active/non-phosphorylated proteins are shown in grey. Data shown in this figure contributed to Supplementary Figure 5 in Cases-Cunillera et al., 2022.

The observation that '2-hit' manipulations used in the present study led to tumors reflecting characteristic human GGs may also have clinically relevant aspects. *BRAF*^{V600E} in human GGs may not be the only relevant genetic alteration in human GGs (Prabowo et al., 2014) but so far undetected mutations with effects on PI3K/mTOR-pathway signaling may be of

relevance. Concerning potential future alternative therapy strategies for GGs, not only for potential $BRAF^{V600E}$-targeting compounds but also mTOR antagonists may be considered.

4.3. Role of *TP53* alteration in the emergence of aGGs

The genetic and molecular profile associated with the rare malignant progression of GGs is not well clarified yet. Some reports have described an association between TP53 dysregulation and malignant progression of GG. However, the *TP53* mutational status in human GGs has been discussed controversially.

The present experiments clearly demonstrated the possibility to elicit experimental murine neoplasms that are neuropathologically virtually indistinguishable from human anaplastic GGs (WHO grade III) based on *Trp53* suppression in the glial cell component as key molecular alteration.

However, in the present system *Trp53* loss represents an initial driver mutation in the generation of neoplasms with malignant GG features and thus the system does not completely reflect the mechanisms underlying the emergence of human malignant GGs. In humans, *TP53* mutation (specifically in exons 5 - 8) has been mainly found in recurring malignant tumors emerging from primary GGs (WHO grade I), lacking *TP53* alterations. These data indicated that mutant *TP53* may not be an initial trigger of the human GG (Hayashi et al., 2001). In line with these data, another case report also showed that loss of heterozygosity affecting the *TP53* gene was only detected in the dedifferentiated GG tissue, but not in the benign and well-differentiated primary GG (Kim et al., 2003).

Furthermore, characterization of benign and malignant tissue from the same GG samples demonstrated that a mutation within the exons 5 – 8 of the *TP53* gene was only present within malignant regions of GG tissue accompanied by an increase of TP53 immunoreactivity only in these areas. This further suggests that this alteration is not required for the initial formation, but rather involved in the progression to anaplastic variants (Pandita et al., 2007). Another study reported the presence of TP53 protein accumulation specifically in the anaplastic component of the tumor with lack of genetic mutations within the exons 4 - 10 of the gene, suggesting the existence of additional

alterations affecting TP53 protein (Suzuki et al., 2002). A recent study demonstrated the presence of *TP53* mutation in a WHO grade I GG (Wang et al., 2016).

In the present study, the loss of *Trp53* was induced as an initial genetic driver together with the expression of *BRAF*^{V600E} and *p*Akt, and therefore does not strictly recapitulate the human scenario in which the additional *TP53* dysregulation appears to be a secondary alteration associated with tumor relapse and progression. The pathogenetic effect of *Trp53* loss during tumor progression may need to be studied with a conditional-controlled system in the present murine tumor models.

4.4. Genetic profile as a determinant of GG tumor growth kinetics and biological behavior

Growth dynamics on tumors arising during development remain still elusive. Tumors induced in mice by only *BRAF*^{V600E} exhibited a very benign biological behavior as the tumor growth was already exhausted at P10. Interestingly, even though we did not find differences in overall survival between *BRAF*^{V600E} and *BRAF*^{V600E}/*p*Akt tumors, we showed that activation of mTOR on *BRAF*^{V600E} GG tumors influenced the tumor growth dynamics in mice by triggering early tumor growth. This is not surprising considering that PI3K/mTOR pathway activation induces protein translation and cell growth, with a critical role during brain development (Crino, 2016). In fact, activation of PI3K/Akt/mTOR pathway has been associated with an increase in cell size and tumor proliferation in GGs (Boer et al., 2010).

Prior studies have investigated the role of mTOR pathway activation in the formation of pediatric brain tumors by using neural stem cells. Alterations in the mTOR pathway function resulted in a reduction of neural stem cell growth, inhibition of astrocyte differentiation and a reduction of gliogenesis (Cloëtta et al., 2013). These data indicated that mTOR activation influenced cell growth in a stemness situation. Moreover, Kaul and colleagues showed that activation of mTOR induced proliferation of neural stem cells harboring mutant KIAA1549:BRAF mutation (Kaul et al., 2012).

These data could well support the *in vivo* results showing that the additional activation of mTOR in embryonic cells harboring *BRAF*^{V600E} led to a premature increase in tumor growth. Tumor-specific immunohistological features could explain this occurrence. The

highly dense glial component in *BRAF*^{V600E}/*p*Akt was defined as tumorigenic since the oncogenic hits were expressed by these cells. In contrast, the astrocytic cells in *BRAF*^{V600E} showed reactive features and the presence of *BRAF*^{V600E} in GFAP-positive cells was almost absent. In this context, the distinct glial nature present in both tumors may partially explain the different growth kinetics.

Despite this distinction in the tumor kinetics at the early stages of tumor development, both *BRAF*^{V600E} and *BRAF*^{V600E}/*p*Akt tumors showed low proliferative potential, as shown by Ki67 immunoreactive index. As a matter of fact, Huse and colleagues demonstrated that Ki67-positive cells in human PLNTY tumors were almost absent (Huse et al., 2017) and the Ki67 labeling index has been found to be around 1 % in human GGs (Blümcke & Wiestler, 2002; Wolf et al., 1994). However, taking into account that cells from the tumor microenvironment (TME) such as immune cells are also able to proliferate, the Ki67 labeling index within the tumor cell population may be even lower and thus requires a deeper examination.

Malignant transformation of GGs is a rare phenomenon, and our present data corroborated the critical relevance of an additional functional loss of the Trp53 protein for the poor biological behavior of *BRAF*^{V600E}/*p*Akt tumors. It has been reported that the proliferation of the glial but not neuronal cell elements triggers the malignant progression of human GGs (Russell & Rubinstein). Our immunohistochemical results showed that *BRAF*^{V600E}/*p*Akt/*Trp53*^{KO} harbored a very dense astroglial component with proliferative potential, suggesting the capability of this cell type of diffusing and migrating to healthy brain tissue.

The malignant biological behavior and invasive growth characteristic shown by *BRAF*^{V600E}/*p*Akt/*Trp53*^{KO} tumors were reflected by its transcriptomic signature. The present data showed a strong enrichment of genes associated with cell proliferation, cell adhesion and extracellular matrix, reflecting the invasive potential of these neoplasms. Radiological examination demonstrated that human aGGs lack well-circumscribed characteristics and presented severe mass effects leading to fundamental alterations in peritumoral regions, such as edemas (Terrier et al., 2017).

Additionally, the presence of necrotic areas has been described in human aGGs and have been considered a requirement for the classification of GG tumor as anaplastic (Demarchi et al., 2011; Terrier et al., 2017). The histological analysis of *BRAF*^{V600E}/*p*Akt/*Trp53*^{KO} tumors also revealed numerous areas of necrosis (data not shown). Furthermore, another criterion used for the classification of human aGG is the presence of microvascular proliferation (Demarchi et al., 2011; Pekmezci et al., 2018; Zanello et al., 2017). These data fit very well with the present results showing an increase in the expression of genes related to angiogenesis in *BRAF*^{V600E}/*p*Akt/*Trp53*^{KO} tumor tissue. In general, both histopathological hallmarks are strongly associated with fast-growing tumors.

Furthermore, immune-related genes appeared overrepresented in *BRAF*^{V600E}/*p*Akt/*Trp53*^{KO} tumors. Interestingly, the differential gene expression led to a GO-term profile of *BRAF*^{V600E}/*p*Akt/*Trp53*^{KO} tumors with strong similarities to human tumors with a mesenchymal profile (Verhaak et al., 2010). This term refers to a subtype of GBM with a high potential of invasion, strong inflammatory reaction, high levels of necrosis, angiogenesis and hypoxia, and generally resistance to therapy. One of the main determinants implicated in the mesenchymal differentiation of brain tumors is the NF-κb transcription factor, which is strongly involved in the regulation of genes related to the immune system, cell survival, proliferation and differentiation. Indeed, results from the present RNA-seq analysis showed a significant abundance of *Nfkb1* in *BRAF*^{V600E}/*p*Akt/*Trp53*^{KO} tumors, compared to control counterparts (data not shown) and thus underlines a high grade of similarity to a specific malignant glioma subtype.

4.5. Clonality implications for the pathogenesis of GGs

There has been an intense debate about whether the dysmorphic neuronal and the neoplastic glial components of GGs derive from one common neural precursor (clonal origin) versus a scenario, in which the tumors develop from a dysmorphic lesion by an independent neoplastic transformation of the glial component (polyclonal origin; (Pandita et al., 2007; Zhu et al., 1997); **Fig. 2**).

Targeting a single neural cell population at E14 with oncogenic hits resulted in brain tumors in adult mice that neuropathologically revealed a prominent dysmorphic ganglionic component admixed to only a sparse fraction of highly differentiated astroglial cells. These

results indicated the emergence of these neoplasms from only one common neural precursor cell population located at the periventricular matrix that has the potential of giving rise to dysmorphic neurons and neoplastic astroglia according to the clonal model (**Fig. 2**). This pathogenetic scenario is well in line with data from human GGs showing *BRAF*^{V600E} expression in dysmorphic neuronal as well as neoplastic glial GG elements (Koelsche et al., 2013).

The 'Brainbow'-approach-based experiments of the present study showed that a clone derived from a single neural precursor cell in *BRAF*^{V600E}/*p*Akt/*Trp53*^{KO} tumors contained both, dysmorphic neurons and neoplastic astroglia indicating that individual GGs represent genetically rather homogeneous but cellularly strongly diverse neoplasms, which is in fundamental contrast to e.g. diffuse gliomas consisting of a cellular population with strong cytological similarities, whereas genetically these cells are rather unstable and thus heterogeneous.

4.6. Excitability aspects of the 1-, 2- and 3-hit GG models

Our data demonstrated a lack of intratumoral hyperexcitability in *BRAF*^{V600E} as well as *BRAF*^{V600E}/*p*Akt/*Trp53*^{KO} tumors. Only the tumor core of *BRAF*^{V600E}/*p*Akt harbored the potential of eliciting spontaneous activity at a comparable level to the preexisting cortex. However, the tissue composition of the control cortex was found to be very distinct from the *BRAF*^{V600E}/*p*Akt tumors. As pointed out above, *BRAF*^{V600E}/*p*Akt tumors were composed of large dysmorphic neurons entrapped within an astroglial fibrillary matrix. Thus, the similar level of spike frequency observed by these two samples represents an intriguing result.

A recent study showed that expression of *BRAF*^{V600E} in radial glial progenitors changed electrophysiological properties of pyramidal neurons, which acquired a highly unusual spiking phenotype(Goz et al., 2020). The intrinsic neuronal excitability triggered by *BRAF*^{V600E} was also reported in the study published by Koh and colleagues. They observed high spike frequencies and increased seizure activity in cortical cells expressing mutant *BRAF*^{V600E} (Koh et al., 2018). These considerations suggest that the highly abundant astroglial component in *BRAF*^{V600E}/*p*Akt may cover the hyperexcitability patterns

derived from *BRAF*^{V600E} neurons in the tumor core, leading to an ultimate spike frequency similar to the control cortex.

Also, after favoring the spike activity with a solution containing low Mg^{2+} and high K^{+}, the activity derived from *BRAF*^{V600E}/*p*Akt tumors was by far the highest compared to the other models in the peritumoral region, suggesting a potential of these tumors to propagate activity to surrounding areas. These considerations prompt the following potential scenario: A preserved *BRAF*^{V600E}/*p*Akt intratumoral spike activity together with the potential to elevate spontaneous activity in surrounding preexisting tissue may trigger higher spike responses.

The almost silenced neuronal activity observed in *BRAF*^{V600E}/*p*Akt/*Trp53*^{KO} and *BRAF*^{V600E} tumor cores correlates with the presence of a high fraction of glial cell elements in both models. The high number of cells positive for oligodendroglial markers in *BRAF*^{V600E} and a large fraction of astroglial elements with proliferative potential within *BRAF*^{V600E}/*p*Akt/*Trp53*^{KO} tumors could explain this outcome.

Moreover, at the transcriptomic level, *BRAF*^{V600E}/*p*Akt/*Trp53*^{KO} revealed a fundamental reduction of synapse-related gene expression, including potassium and calcium channels as well as GABA receptors. Indeed, dysregulation of inhibitory neurotransmission has been already described within areas adjacent to gliomas (Pallud et al., 2014). Thus, the massively disrupted tissue architecture characterized by a reduction in the expression of neuronal-specific genes by the *BRAF*^{V600E}/*p*Akt/*Trp53*^{KO} tumor may explain the lack of neuronal activity as well.

Interestingly, after incubating the slices with aCSF containing low Mg^{2+} and high K^{+}, none of the tumor cores showed an increase in neuronal activity. The lack of potentiation of neuronal activity by external factors is indicative of a loss of cell functionality and a disruption of the network cytoarchitecture in the *BRAF*^{V600E} and *BRAF*^{V600E}/*p*Akt/*Trp53*^{KO} neoplasms, and also a compromise performance by *BRAF*^{V600E}/*p*Akt tumor core.

Overall, these data point to the fact that cellular composition may determine neuronal activity patterns. However, other factors may contribute to increased neuronal hyperexcitability and these aspects will need to be further identified.

4.7. Immunogenic characteristics of mouse GGs – potential impact on neuronal excitability

The dynamic interaction between tumor cells and the TME is highly related to the pathogenesis and biological behavior of neoplasms. Understanding the underlying mechanisms behind their interplay is critical. The immune cells within the TME play a critical role in tumorigenesis. In human GGs, high levels of inflammation with the presence of lymphocytic infiltration have been described as a common feature (Haddad et al., 1992; Smith et al., 1992), and have been found in 70 % of the cases (Dahiya et al., 2013).

4.7.1. Changes in microglial morphology in 2- and 3-hit models as a potential mechanism leading to neuronal network alteration

Both genetically controlled *BRAF*^{V600E}/*p*Akt and *BRAF*^{V600E}/*p*Akt/*Trp53*^{KO} tumor models harbored a high number of microglial cells. Aronica and colleagues demonstrated microglial activation in human GGs associated with chronic epilepsy and found a correlation between the density of activated microglia and epilepsy duration (Aronica et al., 2005). Immunological factors are suggested to play a role in the emergence of epilepsy-related brain tumors, but whether immune infiltration is directly correlated to seizure activity in these neoplasms is still not known.

The present data displayed a dramatic change in the morphology of microglial cells within the *BRAF*^{V600E}/*p*Akt and *BRAF*^{V600E}/*p*Akt/*Trp53*^{KO} tumors in comparison to control tissue. Previous studies have already described changes in microglial shape upon brain injury and a resulting potential alteration of the neuronal network has been suggested. During brain development microglial cells were observed in close contact with neurons and were probed to have a key role in remodeling synaptic processes via phagocytosis to ultimately maintain the CNS homeostasis (Bialas & Stevens, 2013; Nimmerjahn et al., 2005; Schafer et al., 2012; Sierra et al., 2010). Upon a brain insult, microglia cells were shown to have the capability to activate and change the morphology, potentially affecting their interaction with neurons and thereby altering the activity of the neuronal network (Gorter et al., 2006; Liu et al., 2018; Morin-Brureau et al., 2018; Sosunov et al., 2012).

The change in the shape of microglial cells observed within *BRAF*^{V600E}/*p*Akt and *BRAF*^{V600E}/*p*Akt/*Trp53*^{KO} tumors may suggest a noninflammatory contribution of microglial cells via morphological changes leading to alterations in the neuron-microglia communications and thereby determining neuronal activity patterns. These aspects will need to be explored further in detail.

4.7.2. Association between mTOR pathway activation, immune response and seizure activity in GGs

Both 2- and 3-hit mouse models were generated by activation of Akt/mTOR signaling pathway, which has been shown to represent a strong stimulus of innate and adaptive immunity (Thomson et al., 2009). In human GGs, *p*S6 expression and the presence of lymphocyte vascular cuffs were shown to be positively correlated (Prabowo et al., 2014). Interestingly, several studies demonstrated the strong influence of mTOR pathway on T-cell activation and differentiation through modulation of cellular metabolism (reviewed in (Powell et al., 2012)).

Strong evidence associated activation of the mTOR pathway with increased seizure activity in human TSC disorder characterized by hyperactivation of the mTOR signaling pathway (Crino, 2016). An increased mTOR activation has also been reported to determine seizure frequency in experimental models for TSC and focal cortical dysplasia (Crino, 2016; Nguyen et al., 2019). Thus, the immune cell infiltrates following mTOR activation may represent a factor contributing to seizure activity in GGs.

4.8. Conclusions

PI3K pathway activity levels and *Trp53*-loss critically shape neuropathological characteristics, biological behavior, and the electrical activity patterns of $BRAF^{V600E}$-induced tumors. Thus, analyzing the status of mTOR pathway signaling as well as *TP53*-loss/inactivating mutation in $BRAF^{V600E}$-positive human brain tumors may represent reasonable components to be included in diagnostic panels in the future. The animal models presented in this study may be well suited to analyze the effects of new oncological drugs preclinically.

5. Abstract

Background: Developmental, biologically benign brain tumors associated with epilepsy represent a highly heterogeneous group of neoplasms and include glioneuronal and glial entities. Gangliogliomas (GGs) are most abundant in this group. *BRAF*^{V600E} is highly frequent in GGs and activation of mTOR cascade signaling has been reported. Occasional malignant GG variants harbor mutated *TP53*. The improved understanding of the genetic basis and molecular alterations of developmental epilepsy-associated brain tumors in concert with the availability of new transgenic techniques and large-scale omics approaches allows the integrated analyses of pathomechanisms of these neoplasms systematically in novel mouse models.

Aims: Thus, the present study aims to (*1*) develop and characterize *in vivo* tumor models for GGs recapitulating glioneuronal- and epilepsy-associated features, (*2*) understand their subsequent histogenesis and cellular composition, and (*3*) gain knowledge on mechanisms associated with altered excitability.

Results: The present data show that co-electroporation of the constitutively active Akt and mutant *BRAF*^{V600E} transgenes in mouse neural precursors is required to induce low-grade glioneuronal tumors, resembling histopathological features of human GGs including strong microglial infiltrates. These neoplasms arise clonally from a single precursor population, still capable to develop both neuronal and glial cells. Interestingly, the presence of only one transgene does not lead to GG development. Moreover, *Trp53* deletion in this model leads to high-grade glioneuronal tumors with a more severe clinical outcome. Purely glial tumors resembling polymorphous low-grade neuroepithelial tumors of the young (PLNTYs) emerge from only *BRAF*^{V600E}. Spontaneous spike evaluation reflected the highest intrinsic activity potential by tumors harboring both *BRAF*^{V600E} and mTOR activation.

Conclusion: The combinatorial genetic architecture of *BRAF*^{V600E} induced developmental brain tumors with PI3K/Akt/mTOR signaling and *Trp53*-loss determines not only the neuropathological characteristics but also key biological as well as functional features with implication for improving the clinical management of affected patients.

6. List of figures

7. List of tables

8. References

Aghajan, Y., Levy, M. L., Malicki, D. M., & Crawford, J. R. (2016). Novel PPP1CB-ALK fusion protein in a high-grade glioma of infancy. *BMJ Case Reports*, *2016*.

Aguilera, D., Janss, A., Mazewski, C., Castellino, R. C., Schniederjan, M., Hayes, L., Brahma, B., Fogelgren, L., & MacDonald, T. J. (2016). Successful Retreatment of a Child with a Refractory Brainstem Ganglioglioma with Vemurafenib. *Pediatric Blood & Cancer*, *63*(3), 541–543.

Alayev, A., & Holz, M. K. (2013). mTOR Signaling for Biological Control and Cancer. *Journal of Cellular Physiology*, *228*(8), 1658.

Alessi, D. R., James, S. R., Downes, C. P., Holmes, A. B., Gaffney, P. R. J., Reese, C. B., & Cohen, P. (1997). Characterization of a 3-phosphoinositide-dependent protein kinase which phosphorylates and activates protein kinase Balpha. *Current Biology : CB*, *7*(4), 261–269.

Aronica, E., Boer, K., Baybis, M., Yu, J., & Crino, P. (2007). Co-expression of cyclin D1 and phosphorylated ribosomal S6 proteins in hemimegalencephaly. *Acta Neuropathologica*, *114*(3), 287–293.

Aronica, E., Boer, K., Becker, A., Redeker, S., Spliet, W. G. M., van Rijen, P. C., Wittink, F., Breit, T., Wadman, W. J., Lopes da Silva, F. H., Troost, D., & Gorter, J. A. (2008). Gene expression profile analysis of epilepsy-associated gangliogliomas. *Neuroscience*, *151*(1), 272–292.

Aronica, E., Gorter, J. A., Redeker, S., Ramkema, M., Spliet, W. G. M., van Rijen, P. C., Leenstra, S., & Troost, D. (2005). Distribution, characterization and clinical significance of microglia in glioneuronal tumours from patients with chronic intractable epilepsy. *Neuropathology and Applied Neurobiology*, *31*(3), 280–291.

Aronica, E., Leenstra, S., van Veelen, C. W. M., van Rijen, P. C., Hulsebos, T. J., Tersmette, A. C., Yankaya, B., & Troost, D. (2001). Glioneuronal tumors and medically intractable epilepsy: a clinical study with long-term follow-up of seizure outcome after surgery. *Epilepsy Research*, *43*(3), 179–191.

Baulac, S. (2016). mTOR signaling pathway genes in focal epilepsies. *Progress in Brain Research*, *226*, 61–79.

Becker, A. J., Blümcke, I., Urbach, H., Hans, V., & Majores, M. (2006). Molecular neuropathology of epilepsy-associated glioneuronal malformations. *Journal of Neuropathology and Experimental Neurology*, *65*(2), 99–108.

Becker, A. J., Löbach, M., Klein, H., Normann, S., Nöthen, M. M., von Deimling, A., Mizuguchi, M., Elger, C. E., Schramm, J., Wiestler, O. D., & Blümcke, I. (2001). Mutational analysis of TSC1 and TSC2 genes in gangliogliomas. *Neuropathology and Applied Neurobiology*, *27*(2), 105–114.

Bialas, A. R., & Stevens, B. (2013). TGF-β signaling regulates neuronal C1q expression and developmental synaptic refinement. *Nature Neuroscience*, *16*(12), 1773–1782.

Blümcke, I., Aronica, E., Becker, A., Capper, D., Coras, R., Honavar, M., Jacques, T. S., Kobow, K., Miyata, H., Mühlebner, A., Pimentel, J., Söylemezoğlu, F., & Thom, M. (2016). Low-grade epilepsy-associated neuroepithelial tumours - the 2016 WHO classification. *Nature Reviews. Neurology*, *12*(12), 732–740.

Blümcke, I., Giencke, K., Wardelmann, E., Beyenburg, S., Kral, T., Sarioglu, N., Pietsch, T., Wolf, H. K., Schramm, J., Elger, C. E., & Wiestler, O. D. (1999). The CD34 epitope is expressed in neoplastic and malformative lesions associated with chronic, focal epilepsies. *Acta Neuropathologica*, *97*(5), 481–490.

Blumcke, I., Spreafico, R., Haaker, G., Coras, R., Kobow, K., Bien, C. G., Pfäfflin, M., Elger, C., Widman, G., Schramm, J., Becker, A., Braun, K. P., Leijten, F., Baayen, J. C., Aronica, E., Chassoux, F., Hamer, H., Stefan, H., Rössler, K., … Avanzini, G. (2017). Histopathological Findings in Brain Tissue Obtained during Epilepsy Surgery. *The New England Journal of Medicine*, *377*(17), 1648–1656.

Blümcke, I., & Wiestler, O. D. (2002). Gangliogliomas: an intriguing tumor entity associated with focal epilepsies. *Journal of Neuropathology and Experimental Neurology*, *61*(7), 575–584. http://www.ncbi.nlm.nih.gov/pubmed/12125736

Boer, K., Troost, D., Timmermans, W., van Rijen, P. C., Spliet, W. G. M., & Aronica, E. (2010). Pi3K-mTOR signaling and AMOG expression in epilepsy-associated glioneuronal tumors. *Brain Pathology (Zurich, Switzerland)*, *20*(1), 234–244.

Cai, D., Cohen, K. B., Luo, T., Lichtman, J. W., & Sanes, J. R. (2013). Improved tools for the Brainbow toolbox. *Nature Methods*, *10*(6), 540–547.

Cases-Cunillera, S., van Loo, K. M. J., Pitsch, J., Quatraccioni, A., Sivalingam, S., Salomoni, P., Borger, V., Dietrich, D., Schoch, S., & Becker, A. J. (2022). Heterogeneity and excitability of BRAFV600E-induced tumors is determined by Akt/mTOR-signaling state and Trp53-loss. *Neuro-Oncology*, *24*(5).

Cerri, C., Genovesi, S., Allegra, M., Pistillo, F., Püntener, U., Guglielmotti, A., Hugh Perry, V., Bozzi, Y., & Caleo, M. (2016). The Chemokine CCL2 Mediates the Seizure-enhancing Effects of Systemic Inflammation. *The Journal of Neuroscience : The Official Journal of the Society for Neuroscience*, *36*(13), 3777–3788.

Chappé, C., Padovani, L., Scavarda, D., Forest, F., Nanni-Metellus, I., Loundou, A., Mercurio, S., Fina, F., Lena, G., Colin, C., & Figarella-Branger, D. (2013). Dysembryoplastic neuroepithelial tumors share with pleomorphic xanthoastrocytomas and gangliogliomas BRAF(V600E) mutation and expression. *Brain Pathology (Zurich, Switzerland)*, *23*(5), 574–583.

Chen, R., Keoni, C., Waker, C. A., Lober, R. M., & Gutmann, D. H. (2019). KIAA1549-BRAF Expression Establishes a Permissive Tumor Microenvironment Through NFκB-Mediated CCL2 Production. *Neoplasia (New York, N.Y.)*, *21*(1), 52–60.

Cloëtta, D., Thomanetz, V., Baranek, C., Lustenberger, R. M., Lin, S., Oliveri, F., Atanasoski, S., & Rüegg, M. A. (2013). Inactivation of mTORC1 in the developing brain causes microcephaly and affects gliogenesis. *The Journal of Neuroscience : The Official Journal of the Society for Neuroscience*, *33*(18), 7799–7810.

Crino, P. B. (2016). The mTOR signalling cascade: paving new roads to cure neurological disease. *Nature Reviews. Neurology*, *12*(7), 379–392.

Crino, P. B., Aronica, E., Baltuch, G., & Nathanson, K. L. (2010). Biallelic TSC gene inactivation in tuberous sclerosis complex. *Neurology*, *74*(21), 1716.

Dahiya, S., Haydon, D. H., Alvarado, D., Gurnett, C. A., Gutmann, D. H., & Leonard, J. R. (2013). BRAF(V600E) mutation is a negative prognosticator in pediatric ganglioglioma. *Acta Neuropathologica*, *125*(6), 901–910.

Davies, H., Bignell, G. R., Cox, C., Stephens, P., Edkins, S., Clegg, S., Teague, J., Woffendin, H., Garnett, M. J., Bottomley, W., Davis, N., Dicks, E., Ewing, R., Floyd, Y., Gray, K., Hall, S., Hawes, R., Hughes, J., Kosmidou, V., … Futreal, P. A. (2002). Mutations of the BRAF gene in human cancer. *Nature*, *417*(6892), 949–954.

Deb, P., Sharma, M. C., Tripathi, M., Sarat Chandra, P., Gupta, A., & Sarkar, C. (2006). Expression of CD34 as a novel marker for glioneuronal lesions associated with chronic intractable epilepsy. *Neuropathology and Applied Neurobiology*, *32*(5), 461–468.

Demarchi, R., Abu-Abed, S., Munoz, D., & Loch MacDonald, R. (2011). Malignant ganglioglioma: case report and review of literature. *Journal of Neuro-Oncology*, *101*(2), 311–318.

Dobin, A., Davis, C. A., Schlesinger, F., Drenkow, J., Zaleski, C., Jha, S., Batut, P., Chaisson, M., & Gingeras, T. R. (2013). STAR: Ultrafast universal RNA-seq aligner. *Bioinformatics*, *29*(1), 15–21.

Dossi, E., Blauwblomme, T., Nabbout, R., Huberfeld, G., & Rouach, N. (2014). Multi-electrode array recordings of human epileptic postoperative cortical tissue. *Journal of Visualized Experiments : JoVE*, *92*.

Dougherty, M. J., Santi, M., Brose, M. S., Ma, C., Resnick, A. C., Sievert, A. J., Storm, P. B., & Biegel, J. A. (2010). Activating mutations in BRAF characterize a spectrum of pediatric low-grade gliomas. *Neuro-Oncology*, *12*(7), 621–630.

Dudley, R. W. R., Torok, M. R., Gallegos, D. R., Mulcahy-Levy, J. M., Hoffman, L. M., Liu, A. K., Handler, M. H., & Hankinson, T. C. (2015). Pediatric low-grade ganglioglioma: epidemiology, treatments, and outcome analysis on 348 children from the surveillance, epidemiology, and end results database. *Neurosurgery*, *76*(3), 313–319.

Englot, D. J., Berger, M. S., Barbaro, N. M., & Chang, E. F. (2012). Factors associated with seizure freedom in the surgical resection of glioneuronal tumors. *Epilepsia*, *53*(1), 51–57.

Giulioni, M., Gardella, E., Rubboli, G., Roncaroli, F., Zucchelli, M., Bernardi, B., Tassinari, C. A., & Calbucci, F. (2006). Lesionectomy in epileptogenic gangliogliomas: seizure outcome and surgical results. *Journal of Clinical Neuroscience : Official Journal of the Neurosurgical Society of Australasia*, *13*(5), 529–535.

Gorter, J. A., van Vliet, E. A., Aronica, E., Breit, T., Rauwerda, H., Lopes Da Silva, F. H., & Wadman, W. J. (2006). Potential new antiepileptogenic targets indicated by microarray analysis in a rat model for temporal lobe epilepsy. *The Journal of Neuroscience : The Official Journal of the Society for Neuroscience*, *26*(43), 11083–11110.

Goz, R. U., Akgül, G., & LoTurco, J. J. (2020). BRAFV600E expression in neural progenitors results in a hyperexcitable phenotype in neocortical pyramidal neurons. *Journal of Neurophysiology*, *123*(6), 2449–2464.

Gronych, J., Korshunov, A., Bageritz, J., Milde, T., Jugold, M., Hambardzumyan, D., Remke, M., Hartmann, C., Witt, H., Jones, D. T. W., Witt, O., Heiland, S., Bendszus, M., Holland, E. C., Pfister, S., & Lichter, P. (2011). An activated mutant BRAF kinase domain is sufficient to induce pilocytic astrocytoma in mice. *The Journal of Clinical Investigation*, *121*(4), 1344–1348.

Haddad, S. F., Moore, S. A., Menezes, A. H., & Vangilder, J. C. (1992). Ganglioglioma: 13 years of experience. *Neurosurgery*, *31*(2), 171–178.

Hayashi, Y., Iwato, M., Hasegawa, M., Tachibana, O., von Deimling, A., & Yamashita, J. (2001). Malignant transformation of a gangliocytoma/ganglioglioma into a glioblastoma multiforme: a molecular genetic analysis. Case report. *Journal of Neurosurgery*, *95*(1), 138–142.

Hirose, T., Scheithauer, B. W., Lopes, M. B. S., Gerber, H. A., Altermatt, H. J., & VandenBerg, S. R. (1997). Ganglioglioma: an ultrastructural and immunohistochemical study. *Cancer*, *79*(5), 989–1003.

Hollstein, M., Sidransky, D., Vogelstein, B., & Harris, C. C. (1991). p53 mutations in human cancers. *Science (New York, N.Y.)*, *253*(5015), 49–53.

Hsieh, L. S., Wen, J. H., Claycomb, K., Huang, Y., Harrsch, F. A., Naegele, J. R., Hyder, F., Buchanan, G. F., & Bordey, A. (2016). Convulsive seizures from experimental focal cortical dysplasia occur independently of cell misplacement. *Nature Communications 2016 7:1*, *7*(1), 1–12.

Hu, W. H., Ge, M., Zhang, K., Meng, F. G., & Zhang, J. G. (2012). Seizure outcome with surgical management of epileptogenic ganglioglioma: a study of 55 patients. *Acta Neurochirurgica*, *154*(5), 855–861.

Huse, J. T., Snuderl, M., Jones, D. T. W., Brathwaite, C. D., Altman, N., Lavi, E., Saffery, R., Sexton-Oates, A., Blumcke, I., Capper, D., Karajannis, M. A., Benayed, R., Chavez, L., Thomas, C., Serrano, J., Borsu, L., Ladanyi, M., & Rosenblum, M. K. (2017). Polymorphous low-grade neuroepithelial tumor of the young (PLNTY): an epileptogenic neoplasm with oligodendroglioma-like components, aberrant CD34 expression, and genetic alterations involving the MAP kinase pathway. *Acta Neuropathologica*, *133*(3), 417–429.

Iffland, P. H., Baybis, M., Barnes, A. E., Leventer, R. J., Lockhart, P. J., & Crino, P. B. (2018). DEPDC5 and NPRL3 modulate cell size, filopodial outgrowth, and localization of mTOR in neural progenitor cells and neurons. *Neurobiology of Disease*, *114*, 184–193.

Im, S. H., Chung, C. K., Cho, B. K., & Lee, S. K. (2002). Supratentorial ganglioglioma and epilepsy: postoperative seizure outcome. *Journal of Neuro-Oncology*, *57*(1), 59–66.

Kalyan-Raman, U. P., & Olivero, W. C. (1987). Ganglioglioma: a correlative clinicopathological and radiological study of ten surgically treated cases with follow-up. *Neurosurgery*, *20*(3), 428–433.

Kastenhuber, E. R., & Lowe, S. W. (2017). Putting p53 in Context. *Cell*, *170*(6), 1062–1078.

Kaul, A., Chen, Y. H., Emnett, R. J., Dahiya, S., & Gutmann, D. H. (2012). Pediatric glioma-associated KIAA1549:BRAF expression regulates neuroglial cell growth in a cell type-specific and mTOR-dependent manner. *Genes & Development*, *26*(23), 2561.

Kim, N. R., Wang, K. C., Bang, J. S., Choe, G., Park, Y., Kim, S. K., Cho, B. K., & Chi, J. G. (2003). Glioblastomatous transformation of ganglioglioma: case report with reference to molecular genetic and flow cytometric analysis. *Pathology International*, *53*(12), 874–882.

Knight, D. A., Ngiow, S. F., Li, M., Parmenter, T., Mok, S., Cass, A., Haynes, N. M., Kinross, K., Yagita, H., Koya, R. C., Graeber, T. G., Ribas, A., McArthur, G. A., & Smyth, M. J. (2013). Host immunity contributes to the anti-melanoma activity of BRAF inhibitors. *The Journal of Clinical Investigation*, *123*(3), 1371–1381.

Koelsche, C., Wöhrer, A., Jeibmann, A., Schittenhelm, J., Schindler, G., Preusser, M., Lasitschka, F., von Deimling, A., & Capper, D. (2013). Mutant BRAF V600E protein in ganglioglioma is predominantly expressed by neuronal tumor cells. *Acta Neuropathologica*, *125*(6), 891–900.

Koh, H. Y., Kim, S. H., Jang, J., Kim, H., Han, S., Lim, J. S., Son, G., Choi, J., Park, B. O., Heo, W. do, Han, J., Lee, H. J., Lee, D., Kang, H.-C., Shong, M., Paik, S.-B., Kim, D. S., & Lee, J. H. (2018). BRAF somatic mutation contributes to intrinsic epileptogenicity in pediatric brain tumors. *Nature Medicine*, *24*(11), 1662–1668.

Kolk, S. M., de Mooij-Malsen, A. J., & Martens, G. J. M. (2011). Spatiotemporal Molecular Approach of in utero Electroporation to Functionally Decipher Endophenotypes in Neurodevelopmental Disorders. *Frontiers in Molecular Neuroscience*, *4*.

Lafourcade, C. A., Lin, T. v., Feliciano, D. M., Zhang, L., Hsieh, L. S., & Bordey, A. (2013). Rheb Activation in Subventricular Zone Progenitors Leads to Heterotopia, Ectopic Neuronal Differentiation, and Rapamycin-Sensitive Olfactory Micronodules and Dendrite Hypertrophy of Newborn Neurons. *The Journal of Neuroscience*, *33*(6), 2419.

Lane, D. P. (1992). Cancer. p53, guardian of the genome. *Nature*, *358*(6381), 15–16.

Lang, F. F., Epstein, F. J., Ransohoff, J., Allen, J. C., Wisoff, J., Abbott, I. R., & Miller, D. C. (1993). Central nervous system gangliogliomas. Part 2: Clinical outcome. *Journal of Neurosurgery*, *79*(6), 867–873.

Laplante, M., & Sabatini, D. M. (2009). mTOR signaling at a glance. *Journal of Cell Science*, *122*(Pt 20), 3589–3594.

Liao, Y., Smyth, G. K., & Shi, W. (2013). The Subread aligner: fast, accurate and scalable read mapping by seed-and-vote. *Nucleic Acids Research*, *41*(10), e108.

Liao, Y., Smyth, G. K., & Shi, W. (2014). FeatureCounts: An efficient general purpose program for assigning sequence reads to genomic features. *Bioinformatics*, *30*(7), 923–930.

Lieberman, N. A. P., Degolier, K., Kovar, H. M., Davis, A., Hoglund, V., Stevens, J., Winter, C., Deutsch, G., Furlan, S. N., Vitanza, N. A., Leary, S. E. S., & Crane, C. A. (2019). Characterization of the immune microenvironment of diffuse intrinsic pontine glioma: implications for development of immunotherapy. *Neuro-Oncology*, *21*(1), 83–94.

Liu, J. Y. W., Matarin, M., Reeves, C., McEvoy, A. W., Miserocchi, A., Thompson, P., Sisodiya, S. M., & Thom, M. (2018). Doublecortin-expressing cell types in temporal lobe epilepsy. *Acta Neuropathologica Communications*, *6*(1), 60.

Livet, J., Weissman, T. A., Kang, H., Draft, R. W., Lu, J., Bennis, R. A., Sanes, J. R., & Lichtman, J. W. (2007). Transgenic strategies for combinatorial expression of fluorescent proteins in the nervous system. *Nature*, *450*(7166), 56–62.

Io Turco, J., Manent, J. B., & Sidiqi, F. (2009). New and improved tools for in utero electroporation studies of developing cerebral cortex. *Cerebral Cortex (New York, N.Y. : 1991)*, *19 Suppl 1*(Suppl 1).

Louis, D. N., Ohgaki, H., Wiestler, O. D., Cavenee, W. K., Burger, P. C., Jouvet, A., Scheithauer, B. W., & Kleihues, P. (2007). The 2007 WHO classification of tumours of the central nervous system. *Acta Neuropathologica*, *114*(2), 97–109.

Louis, D. N., Perry, A., Reifenberger, G., von Deimling, A., Figarella-Branger, D., Cavenee, W. K., Ohgaki, H., Wiestler, O. D., Kleihues, P., & Ellison, D. W. (2016). The 2016 World Health Organization Classification of Tumors of the Central Nervous System: a summary. *Acta Neuropathologica*, *131*(6), 803–820.

Louis, D. N., Perry, A., Wesseling, P., Brat, D. J., Cree, I. A., Figarella-Branger, D., Hawkins, C., Ng, H. K., Pfister, S. M., Reifenberger, G., Soffietti, R., von Deimling, A., & Ellison, D. W. (2021). The 2021 WHO Classification of Tumors of the Central Nervous System: a summary. *Neuro-Oncology*, *23*(8), 1231–1251.

Luyken, C., Blümcke, I., Fimmers, R., Urbach, H., Wiestler, O. D., & Schramm, J. (2004). Supratentorial gangliogliomas: Histopathologic grading and tumor recurrence in 184 patients with a median follow-up of 8 years. *Cancer*, *101*(1), 146–155.

Miller, D. C., Lang, F. F., & Epstein, F. J. (1993). Central nervous system gangliogliomas. Part 1: Pathology. *Journal of Neurosurgery*, *79*(6), 859–866.

Morin-Brureau, M., Milior, G., Royer, J., Chali, F., LeDuigou, C., Savary, E., Blugeon, C., Jourdren, L., Akbar, D., Dupont, S., Navarro, V., Baulac, M., Bielle, F., Mathon, B., Clemenceau, S., & Miles, R. (2018). Microglial phenotypes in the human epileptic temporal lobe. *Brain : A Journal of Neurology*, *141*(12), 3343–3360.

Morris, H. H., Estes, M. L., Gilmore, R., van Ness, P. C., Barnett, G. H., & Turnbull, J. (1993). Chronic intractable epilepsy as the only symptom of primary brain tumor. *Epilepsia*, *34*(6), 1038–1043.

Nguyen, L. H., Mahadeo, T., & Bordey, A. (2019). mTOR Hyperactivity Levels Influence the Severity of Epilepsy and Associated Neuropathology in an Experimental Model of Tuberous Sclerosis Complex and Focal Cortical Dysplasia. *The Journal of Neuroscience : The Official Journal of the Society for Neuroscience*, *39*(14), 2762–2773.

Nimmerjahn, A., Kirchhoff, F., & Helmchen, F. (2005). Resting microglial cells are highly dynamic surveillants of brain parenchyma in vivo. *Science (New York, N.Y.)*, *308*(5726), 1314–1318.

Nishio, S., Morioka, T., Mihara, F., Gondo, K., & Fukui, M. (2001). Cerebral ganglioglioma with epilepsy: neuroimaging features and treatment. *Neurosurgical Review*, *24*(1), 14–19.

Pallud, J., Audureau, E., Blonski, M., Sanai, N., Bauchet, L., Fontaine, D., Mandonnet, E., Dezamis, E., Psimaras, D., Guyotat, J., Peruzzi, P., Page, P., Gal, B., Párraga, E., Baron, M. H., Vlaicu, M., Guillevin, R., De'aux, B., Duffau, H., … Huberfeld, G. (2014). Epileptic seizures in diffuse low-grade gliomas in adults. *Brain : A Journal of Neurology*, *137*(Pt 2), 449–462.

Pallud, J., Capelle, L., & Huberfeld, G. (2013). Tumoral epileptogenicity: how does it happen? *Epilepsia*, *54 Suppl 9*(SUPPL. 9), 30–34.

Pandita, A., Balasubramaniam, A., Perrin, R., Shannon, P., & Guha, A. (2007). Malignant and benign ganglioglioma: A pathological and molecular study. *Neuro-Oncology*, *9*(2), 124–134.

Pekmezci, M., Villanueva-Meyer, J. E., Goode, B., van Ziffle, J., Onodera, C., Grenert, J. P., Bastian, B. C., Chamyan, G., Maher, O. M., Khatib, Z., Kleinschmidt-DeMasters, B. K., Samuel, D., Mueller, S., Banerjee, A., Clarke, J. L., Cooney, T., Torkildson, J.,

Gupta, N., Theodosopoulos, P., … Solomon, D. A. (2018). The genetic landscape of ganglioglioma. *Acta Neuropathologica Communications*, *6*(1), 47.

Powell, J. D., Pollizzi, K. N., Heikamp, E. B., & Horton, M. R. (2012). Regulation of Immune Responses by mTOR. *Annual Review of Immunology*, *30*, 39.

Prabowo, A. S., Iyer, A. M., Veersema, T. J., Anink, J. J., Schouten-van Meeteren, A. Y. N., Spliet, W. G. M., van Rijen, P. C., Ferrier, C. H., Capper, D., Thom, M., & Aronica, E. (2014). BRAF V600E mutation is associated with mTOR signaling activation in glioneuronal tumors. *Brain Pathology (Zurich, Switzerland)*, *24*(1), 52–66.

Prabowo, A. S., van Scheppingen, J., Iyer, A. M., Anink, J. J., Spliet, W. G. M., van Rijen, P. C., Meeteren, A. Y. N. S. van, & Aronica, E. (2015). Differential expression and clinical significance of three inflammation-related microRNAs in gangliogliomas. *Journal of Neuroinflammation*, *12*(1).

Prayson, R. A., & Gales, J. M. (2015). Coexistent ganglioglioma, focal cortical dysplasia, and hippocampal sclerosis (triple pathology) in chronic epilepsy. *Annals of Diagnostic Pathology*, *19*(5), 310–313.

Rak, B., Szlufik, S., Grajkowska, W., Perek, D., Dembowska-Bagińska, B., Filipek, I., Daszkiewicz, P., Włodarski, P., & Jóźwiak, J. (2013). Upregulation of mitogen-activated protein kinase in ganglioglioma. *Folia Neuropathologica*, *51*(4), 283–289.

Reinartz, S., Biro, I., Gal, A., Giugliano, M., & Marom, S. (2014). Synaptic dynamics contribute to long-term single neuron response fluctuations. *Frontiers in Neural Circuits*, *8*(JULY).

Richie, C. T., Whitaker, L. R., Whitaker, K. W., Necarsulmer, J., Baldwin, H. A., Zhang, Y., Fortuno, L., Hinkle, J. J., Koivula, P., Henderson, M. J., Sun, W., Wang, K., Smith, J. C., Pickel, J., Ji, N., Hope, B. T., & Harvey, B. K. (2017). Near-infrared fluorescent protein iRFP713 as a reporter protein for optogenetic vectors, a transgenic Cre-reporter rat, and other neuronal studies. *Journal of Neuroscience Methods*, *284*, 1–14.

Ritchie, M. E., Phipson, B., Wu, D., Hu, Y., Law, C. W., Shi, W., & Smyth, G. K. (2015). Limma powers differential expression analyses for RNA-sequencing and microarray studies. *Nucleic Acids Research*, *43*(7), e47.

Ritterhouse, L. L., & Barletta, J. A. (2015). BRAF V600E mutation-specific antibody: A review. *Seminars in Diagnostic Pathology*, *32*(5), 400–408.

Robinson, J. P., VanBrocklin, M. W., Guilbeault, A. R., Signorelli, D. L., Brandner, S., & Holmen, S. L. (2010). Activated BRAF induces gliomas in mice when combined with Ink4a/Arf loss or Akt activation. *Oncogene*, *29*(3), 335–344.

Robinson., McCarthy, D., & Smyth, G. (2010). edgeR: a Bioconductor package for differential expression analysis of digital gene expression data. *Bioinformatics (Oxford, England)*, *26*(1), 139–140.

Roux, P. P., Shahbazian, D., Vu, H., Holz, M. K., Cohen, M. S., Taunton, J., Sonenberg, N., & Blenis, J. (2007). RAS/ERK Signaling Promotes Site-specific Ribosomal Protein S6 Phosphorylation via RSK and Stimulates Cap-dependent Translation. *The Journal of Biological Chemistry*, *282*(19), 14056.

Rumana, C. S., & Valadka, A. B. (1998). Radiation therapy and malignant degeneration of benign supratentorial gangliogliomas. *Neurosurgery*, *42*(5), 1038–1043.

Russell D S, & Rubinstein L J. (1962). *Ganglioglioma: a case with long history and malignant evolution - PubMed*. https://pubmed.ncbi.nlm.nih.gov/14495410/

Saad, A. G., Jayarao, M., Chin, L. S., & Delalle, I. (2008). Ganglioglioma associated with cerebral cortical dysplasia: an unusual case with extensive leptomeningeal involvement. *Pediatric and Developmental Pathology : The Official Journal of the Society for Pediatric Pathology and the Paediatric Pathology Society*, *11*(6), 474–478.

Samadani, U., Judkins, A. R., Akpalu, A., Aronica, E., & Crino, P. B. (2007). Differential cellular gene expression in ganglioglioma. *Epilepsia*, *48*(4), 646–653.

Sánchez-Alegría, K., Flores-León, M., Avila-Muñoz, E., Rodríguez-Corona, N., & Arias, C. (2018). PI3K Signaling in Neurons: A Central Node for the Control of Multiple Functions. *International Journal of Molecular Sciences*, *19*(12).

Sarbassov, D. D., Guertin, D. A., Ali, S. M., & Sabatini, D. M. (2005). Phosphorylation and regulation of Akt/PKB by the rictor-mTOR complex. *Science (New York, N.Y.)*, *307*(5712), 1098–1101.

Schafer, D. P., Lehrman, E. K., Kautzman, A. G., Koyama, R., Mardinly, A. R., Yamasaki, R., Ransohoff, R. M., Greenberg, M. E., Barres, B. A., & Stevens, B. (2012). Microglia sculpt postnatal neural circuits in an activity and complement-dependent manner. *Neuron*, *74*(4), 691–705.

Schick, V., Majores, M., Engels, G., Hartmann, W., Elger, C. E., Schramm, J., Schoch, S., & Becker, A. J. (2007). Differential Pi3K-pathway activation in cortical tubers and focal cortical dysplasias with balloon cells. *Brain Pathology (Zurich, Switzerland)*, *17*(2), 165–173.

Schindler, G., Capper, D., Meyer, J., Janzarik, W., Omran, H., Herold-Mende, C., Schmieder, K., Wesseling, P., Mawrin, C., Hasselblatt, M., Louis, D. N., Korshunov, A., Pfister, S., Hartmann, C., Paulus, W., Reifenberger, G., & von Deimling, A. (2011). Analysis of BRAF V600E mutation in 1,320 nervous system tumors reveals high mutation frequencies in pleomorphic xanthoastrocytoma, ganglioglioma and extra-cerebellar pilocytic astrocytoma. *Acta Neuropathologica*, *121*(3), 397–405.

Schramm, J., Kral, T., Grunwald, T., & Blümcke, I. (2001). Surgical treatment for neocortical temporal lobe epilepsy: clinical and surgical aspects and seizure outcome. *Journal of Neurosurgery*, *94*(1), 33–42.

Selvanathan, S. K., Hammouche, S., Salminen, H. J., & Jenkinson, M. D. (2011). Outcome and prognostic features in anaplastic ganglioglioma: analysis of cases from the SEER database. *Journal of Neuro-Oncology*, *105*(3), 539–545.

Siddiqi, F., Chen, F., Aron, A. W., Fiondella, C. G., Patel, K., & LoTurco, J. J. (2014). Fate mapping by piggyBac transposase reveals that neocortical GLAST+ progenitors

generate more astrocytes than Nestin+ progenitors in rat neocortex. *Cerebral Cortex (New York, N.Y. : 1991)*, *24*(2), 508–520.

Sierra, A., Encinas, J. M., Deudero, J. J. P., Chancey, J. H., Enikolopov, G., Overstreet-Wadiche, L. S., Tsirka, S. E., & Maletic-Savatic, M. (2010). Microglia shape adult hippocampal neurogenesis through apoptosis-coupled phagocytosis. *Cell Stem Cell*, *7*(4), 483–495.

Silver, J. M., Rawlings, C. E., Rossitch, E., Zeidman, S. M., & Friedman, A. H. (1991). Ganglioglioma: a clinical study with long-term follow-up. *Surgical Neurology*, *35*(4), 261–266.

Smith, N. M., Carli, M. M., Hanieh, A., Clark, B., Bourne, A. J., & Byard, R. W. (1992). Gangliogliomas in childhood. *Child's Nervous System : ChNS : Official Journal of the International Society for Pediatric Neurosurgery*, *8*(5), 258–262.

Sokolov, A. M., Seluzicki, C. M., Morton, M. C., & Feliciano, D. M. (2018). Dendrite growth and the effect of ectopic Rheb expression on cortical neurons. *Neuroscience Letters*, *671*, 140–147.

Sommer, B., Wimmer, C., Coras, R., Blumcke, I., Lorber, B., Hamer, H. M., Stefan, H., Buchfelder, M., & Roessler, K. (2015). Resection of cerebral gangliogliomas causing drug-resistant epilepsy: short- and long-term outcomes using intraoperative MRI and neuronavigation. *Neurosurgical Focus*, *38*(1).

Sosunov, A. A., Wu, X., McGovern, R. A., Coughlin, D. G., Mikell, C. B., Goodman, R. R., & McKhann, G. M. (2012). The mTOR pathway is activated in glial cells in mesial temporal sclerosis. *Epilepsia*, *53 Suppl 1*(SUPPL. 1), 78–86.

Sutton, L. N., Packer, R. J., Rorke, L. B., Bruce, D. A., & Schut, L. (1983). Cerebral gangliogliomas during childhood. *Neurosurgery*, *13*(2), 124–128.

Suzuki, H., Otsuki, T., Iwasaki, Y., Katakura, R., Asano, H., Tadokoro, M., Suzuki, Y., Tezuka, F., & Takei, H. (2002). Anaplastic ganglioglioma with sarcomatous component: an immunohistochemical study and molecular analysis of p53 tumor

suppressor gene. *Neuropathology : Official Journal of the Japanese Society of Neuropathology*, *22*(1), 40–47.

Suzuki, Y., Shirai, K., Oka, K., Mobaraki, A., Yoshida, Y., Noda, S., Okamoto, M., Suzuki, Y., Itoh, J., Itoh, H., Ishiuchi, S., & Nakano, T. (2010). Higher pAkt expression predicts a significant worse prognosis in glioblastomas. *Journal of Radiation Research*, *51*(3), 343–348. http://www.ncbi.nlm.nih.gov/pubmed/20410674

Taylor, D. C., Falconer, M. A., Bruton, C. J., & Corsellis, J. A. (1971). Focal dysplasia of the cerebral cortex in epilepsy. *Journal of Neurology, Neurosurgery, and Psychiatry*, *34*(4), 369–387.

Terrier, L. M., Bauchet, L., Rigau, V., Amelot, A., Zouaoui, S., Filipiak, I., Caille, A., Almairac, F., Aubriot-Lorton, M. H., Bergemer-Fouquet, A. M., Bord, E., Cornu, P., Czorny, A., Dam Hieu, P., Debono, B., Delisle, M. B., Emery, E., Farah, W., Gauchotte, G., … Zemmoura, I. (2017). Natural course and prognosis of anaplastic gangliogliomas: a multicenter retrospective study of 43 cases from the French Brain Tumor Database. *Neuro-Oncology*, *19*(5), 678–688.

Thom, M., Blümcke, I., & Aronica, E. (2012). Long-term epilepsy-associated tumors. *Brain Pathology (Zurich, Switzerland)*, *22*(3), 350–379.

Thom, M., Martinian, L., Sen, A., Cross, J. H., Harding, B. N., & Sisodiya, S. M. (2005). Cortical neuronal densities and lamination in focal cortical dysplasia. *Acta Neuropathologica*, *110*(4), 383–392.

Thomas, G., Martin-Perez, J., Siegmann, M., & Otto, A. M. (1982). The effect of serum, EGF, PGF2 alpha and insulin on S6 phosphorylation and the initiation of protein and DNA synthesis. *Cell*, *30*(1), 235–242.

Thomson, A. W., Turnquist, H. R., & Raimondi, G. (2009). Immunoregulatory functions of mTOR inhibition. *Nature Reviews. Immunology*, *9*(5), 324–337.

Verhaak, R. G. W., Hoadley, K. A., Purdom, E., Wang, V., Qi, Y., Wilkerson, M. D., Miller, C. R., Ding, L., Golub, T., Mesirov, J. P., Alexe, G., Lawrence, M., O'Kelly, M.,

Tamayo, P., Weir, B. A., Gabriel, S., Winckler, W., Gupta, S., Jakkula, L., … Hayes, D. N. (2010). An integrated genomic analysis identifies clinically relevant subtypes of glioblastoma characterized by abnormalities in PDGFRA, IDH1, EGFR and NF1. *Cancer Cell*, *17*(1), 98.

Wan, P. T. C., Garnett, M. J., Roe, S. M., Lee, S., Niculescu-Duvaz, D., Good, V. M., Project, C. G., Jones, C. M., Marshall, C. J., Springer, C. J., Barford, D., & Marais, R. (2004). Mechanism of activation of the RAF-ERK signaling pathway by oncogenic mutations of B-RAF. *Cell*, *116*(6), 855–867.

Wang, J. L., Hong, C. S., Otero, J., Puduvalli, V. K., & Elder, J. B. (2016). Genetic Characterization of a Multifocal Ganglioglioma Originating Within the Spinal Cord. *World Neurosurgery*, *96*, 608.e1.

Wolf, H. K., Müller, M. B., Spänle, M., Zentner, J., Schramm, J., & Wiestler, O. D. (1994). Ganglioglioma: a detailed histopathological and immunohistochemical analysis of 61 cases. *Acta Neuropathologica*, *88*(2), 166–173. http://www.ncbi.nlm.nih.gov/pubmed/7985497

Wolf, H. K., Roos, D., Blümcke, I., Pietsch, T., & Wiestler, O. D. (1996). Perilesional neurochemical changes in focal epilepsies. *Acta Neuropathologica*, *91*(4), 376–384.

Zanello, M., Pagès, M., Roux, A., Peeters, S., Dezamis, E., Puget, S., Devaux, B., Sainte-Rose, C., Zerah, M., Louvel, G., Dumont, S. N., Meder, J.-F., Grill, J., Huberfeld, G., Chrétien, F., Parraga, E., Sauvageon, X., Varlet, P., & Pallud, J. (2017). Epileptic seizures in anaplastic gangliogliomas. *British Journal of Neurosurgery*, *31*(2), 227–233.

Zentner, J., Wolf, H. K., Ostertun, B., Hufnagel, A., Campos, M. G., Solymosi, L., & Schramm, J. (1994). Gangliogliomas: clinical, radiological, and histopathological findings in 51 patients. *Journal of Neurology, Neurosurgery, and Psychiatry*, *57*(12), 1497–1502.

Zhang, D., Henning, T. D., Zou, L. G., Hu, L. B., Wen, L., Feng, X. Y., Dai, S. H., Wang, W. X., Sun, Q. R., & Zhang, Z. G. (2008). Intracranial ganglioglioma: clinicopathological and MRI findings in 16 patients. *Clinical Radiology*, *63*(1), 80–91.

Zhu, J. J., Leon, S. P., Folkerth, R. D., Guo, S. Z., Wu, J. K., & Black, P. M. (1997). Evidence for clonal origin of neoplastic neuronal and glial cells in gangliogliomas. *The American Journal of Pathology*, *151*(2), 565–571. http://www.ncbi.nlm.nih.gov/pubmed/9250169

9. Acknowledgements

I would like to thank the following people without whom I would not have made it through my PhD.

First and foremost, I would like to thank my supervisors, Susanne Schoch and Albert Becker. I would like to thank Susanne for being always accessible and willing to help me in all steps of my project and for offering me advice and encouragement throughout my years as a PhD. I would like to thank my supervisor Albert Becker for his guidance through this project. This PhD project as well as my main publication would have never been accomplished without his involvement, dedication, and support. Both of them provided brilliant guidance in my transition from student to academic. I would also like to thank them for being extremely supportive with personal issues. I will always appreciate this support.

My sincere thanks to Julika Pitsch for her invaluable assistance and insights during all these years, for always being willing to share her knowledge with me and for offering her help in many ways since the first day. Very special thanks also to Karen van Loo for helping me to put the manuscript together and whose expertise pushed me to improve my thinking and knowledge.

I am very thankful also for all committee members, who took the time to give me their feedback and corrections on my thesis. I appreciate their dedication and professional advice.

I would like to give special thanks to my friend Anne Quatraccioni for the endless amount of support and for helping me numerous times unconditionally. I am extremely grateful for having shared my PhD experience with her so closely. Getting through this period as PhD required more than professional support and she was also the person I could always count on at any moment for anything.

I also want to express my deepest gratitude to my old and current lab colleagues. All of them made my study and life in the lab a wonderful time and my special thanks go to Barbara, Polina, Alex, Julia K., Sara, Vicky, Pia S., Eva, Julia B., Monika, Sabine, Pia T.,

Marie, Vivian, Annachiara, Annika, Idil, Despina, Jorge, Daniel, Delara, Philipp, Aya, Katrin, Shayne, Katia, and Gunther.

Especially I would particularly like to single out Sabine and Pia for their technical assistance in my study. Without their help, I would not have been able to build my thesis as it is.

I am grateful to my parents, Jaume and Rosa, who have always trusted in me and supported me from …. Km away and taught me the important values in this life. Without their unconditional love and values I would not be the person I am today. My deepest thanks to my brother Jaume, who has been my closest life partner and whose moral support has been the biggest comfort to deal with the past academic years. I am also very proud of him for starting a PhD as well. I also want to express my gratitude to my grandparents, Elena and Josep for their tremendous understanding and encouragement throughout my studies. I thank them for their belief in me.

A profound thank you must go to my boyfriend, Philipp, for the endless amount of support, love, encouragement, caring and unconditional friendship. I thank him to help me to overcome the difficulties, especially during these last months. Without him holding my hand, it would have been difficult to stand up again. I am indebted to him.

I would like to extend my sincere thanks to my friends, for encouraging and supporting me whenever I needed them, and for providing me with happy distractions, which helped to rest my mind outside of my research. Special thanks to Anna, Marta, Eduard, Gerard, Alex, Aleix, Neil, Elena, Álvaro, Adrià, and Laia for sharing their life with me outside the lab and giving me advice and moral support through all situations. Many thanks also to my rugby mates for the empowering friendship and energy, which definitely had a huge positive impact on the course of my PhD.

Finally, my friend Sergi deserves my deepest respect and love. Wherever you are, I am thankful to you for being a true friend! You will always be in my heart and a part of myself.